

# FRANZ: Framework for analytical one-zone blastwave dynamics

Leonard E. C. Romano<sup>1,2,3,\*</sup>

<sup>1</sup> Excellence Cluster ORIGINS, Boltzmannstr. 2, 85748 Garching, Germany

<sup>2</sup> European Southern Observatory (ESO), Karl-Schwarzschild-Straße 2, 85748 Garching, Germany

<sup>3</sup> Universitäts-Sternwarte, Fakultät für Physik, Ludwig-Maximilians-Universität München, Scheinerstr. 1, 81679 München, Germany

July 7, 2026

## ABSTRACT

*Context.* Supernova remnants (SNRs) and superbubbles (SBs) evolve in complex galactic environments shaped by various different processes. While classical modeling approaches successfully describe blastwaves in uniform media, a unified framework capable of treating these environmental effects simultaneously has been lacking.

*Aims.* We develop a flexible analytical framework for modeling blastwave evolution in arbitrary environments and use it to investigate how large-scale galactic structure affects the dynamics and morphology of evolved SNRs and SBs.

*Methods.* We introduce FRANZ (FRamework for ANalytical one-Zone blastwave dynamics), a modular thin-shell model that follows the local evolution of a shock-surface segment in environments characterized by arbitrary density, velocity and gravitational fields. After validating the model against well-established analytical results, we apply it to study the effects of vertical stratification, galactic shear and dense galactic substructure on blastwave evolution.

*Results.* FRANZ reproduces the classical evolution of blastwaves in uniform media while extending to complex environments. We derive criteria for disk break out in stratified media, characterize the timescales on which differential rotation deforms blastwaves and identify a new mechanism, by which it can suppress the momentum coupling in continuously-driven blastwaves. Interactions with dense filaments modify both shock-surface morphology and dynamics and confound the interpretation of the expansion history of observed remnants, which depends on the density distribution prior to the onset of explosions, which is fundamentally inaccessible from the observed state. In highly structured media with a high volume-filling factor of diffuse gas, ages inferred from the observed state may be systematically overestimated.

*Conclusions.* FRANZ provides a computationally inexpensive and extensible framework for studying blastwaves in realistic galactic environments. It offers a useful complement to numerical simulations for interpreting observations of evolved SNRs and SBs and for developing improved models of stellar feedback in large-scale simulations.

**Key words.** ISM: bubbles – ISM: structure – ISM: supernova remnants - Shock waves – methods: analytical

## 1. Introduction

The environment in which supernovae (SNe) explode is neither stationary nor homogeneous. Observations of Galactic supernova remnants (SNRs) reveal complex characteristics that are commonly attributed to interactions with structured circumstellar (e.g., Kobashi et al. 2024; De Looze et al. 2024) and interstellar media (e.g. Arias et al. 2018; Deng et al. 2023; Paylı et al. 2024), while extragalactic observations indicate that large-scale gas flows and gravity can further influence their evolution (Watkins et al. 2023).

Although numerical studies can reproduce the properties of individual remnants, such as G1.9+0.3 (Zhang et al. 2023), G332.5-5.6, G290.1-0.8 (Velázquez et al. 2023), Pa 30 (Duffell et al. 2024), and the Local Bubble (Breitschwerdt & de Avillez 2006; Breitschwerdt et al. 2016), analytical models generally assume expansion into uniform, stationary media (e.g. Ostriker & McKee 1988; Truelove & McKee 1999; El-Badry et al. 2019). Only a limited number of studies have explored departures from this idealization (e.g., Laumbach & Probst 1969; Haid et al. 2016; Jiménez et al. 2024; Lau & Bonnell 2025).

These analytical models provide a well-established evolutionary picture in which SNRs progress from free ex-

pansion (Truelove & McKee 1999) through the Sedov-Taylor phase (Taylor 1950; Sedov 1959) before radiative losses lead to shell formation and subsequent snowplow evolution (Cioffi et al. 1988; Kim & Ostriker 2015; Fierlinger et al. 2016), ultimately merging with the ISM (Slavin & Cox 1992; Romano et al. 2024) or contributing to the formation of superbubbles (SBs; e.g., El-Badry et al. 2019; Oku et al. 2022). While this framework successfully describes idealized environments, its applicability to structured galactic media shaped by turbulence, differential rotation and gravity remains uncertain.

Previous analytical studies have typically considered individual environmental effects in isolation. Vertical stratification has been shown to accelerate adiabatic blastwaves after atmospheric breakout, although these calculations generally neglect radiative cooling and gravity, which become important on comparable timescales (Kompaneets 1960; Laumbach & Probst 1969; Moellenhoff 1976; Koo & McKee 1990). Differential rotation deforms SNRs into elongated morphologies over a fraction of an orbital period and may explain the shapes of observed superbubbles (Tenorio-Tagle & Palous 1987; Bisnovatyi-Kogan & Silich 1995; Palouš et al. 2020; Jiménez et al. 2024).

The effects of turbulent density fluctuations and small-scale low-density channels have likewise been investigated (Haid et al. 2016; Lau & Bonnell 2025). These studies suggest that turbulence only weakly modifies the average radial momentum of

\* Corresponding author: Leonard E. C. Romano  
e-mail: lromano@usm.lmu.de

SNRs, whereas localized channels can substantially alter the coupling of SN feedback to the surrounding ISM. A unified analytical framework that incorporates these mechanisms simultaneously is, however, still lacking.

In a recent paper (Henceforth RBB25 Romano et al. 2025a) we introduced the SSSI (Supernovae In a Stratified, Shearing ISM) simulations, in which we study the evolution of SNRs in a realistic galactic environment. There we have found that, while the dynamics of young and small SNRs are well described by the simple analytic models based on SNe exploding in a uniform, stationary ISM, once they reach a certain age ( $\gtrsim 1$  Myr) and size ( $\gtrsim 100$  pc) SNRs begin to deviate from the classical theory, likely due to the above mentioned processes. Thus, in order to better understand the dynamics of such large and old SNRs, a comprehensive model that takes all of these effects into account is needed.

In this paper we introduce a FRamework for ANalytical one-Zone blastwave dynamics (FRANZ) in order to model the the dynamics of SNRs in complex environments, taking into account the findings of RBB25. The model aims to lay out the theoretical foundations for the study of SNRs in complex geometries and serve as a simple tool for exploring the effects of previously unexplored phenomena on SNR dynamics, without the need of computationally challenging and expensive numerical simulations. To achieve this goal we aimed to formulate the model in a modular way, that easily allows for the inclusion of new phenomena.

The remainder of this paper is organized as follows. In Sec. 2 we describe our model. In Sec. 3 we apply the model to a number of complex settings, in order to investigate their individual effects on SNR evolution. In Sec.4 we discuss some of the limitations and future directions of the model. We close in Sec. 5 summarizing our results. In the Appendix we provide some additional background to some aspects of our model and evaluate how well it reproduces a number of well established results.

## 2. The FRANZ model

We introduce the FRANZ<sup>1</sup> model for the expansion of a blastwave powered by central energy- and mass-injection. The blastwave is expanding into an arbitrary medium characterized by density-, velocity- and (gravitational) acceleration fields, denoted  $\rho_0(\mathbf{r}, t)$ ,  $\mathbf{v}_{\text{ext}}(\mathbf{r}, t)$  and  $\mathbf{g}(\mathbf{r}, t)$ , respectively. Our model solves the blastwave equation of motion (Ostriker & McKee 1988) using the thin-shell and sector approximations (Laumbach & Probst 1969). It follows the one-zone dynamics of a shell-segment per unit angle (i.e. along a single streamline) by assuming that all of the swept-up mass along the streamline is incorporated into an infinitesimally thin shell. Similarly to other models using the thin-shell approximation (e.g. Bisnovaty-Kogan & Silich 1995; Palouš et al. 2020; Jiménez et al. 2024), we model the curving of streamlines due to normal accelerations, but instead of requiring to evolve the whole shock-surface simultaneously, we opt for an entirely local approach.

The expanding shell segment originates from the explosion center  $\mathbf{r}_{\text{expl}}$  and is associated with its initial expansion direction  $\hat{\mathbf{e}} = (\sin \theta \cos \phi, \sin \theta \sin \phi, \cos \theta)$ . We use a HEALPIX tessellation of the unit sphere (Górski et al. 2005) to uniformly sample all directions.

The dynamics of the shell-segments traced by their position  $\mathbf{r}_s(t)$ , expansion velocity  $\mathbf{v}_s(t)$ , mass  $M(t)$  and energy  $E(t)$  are

<sup>1</sup> The FRANZ code is made publicly available at <https://zenodo.org/records/21180994>.

**Table 1.** Constants in Eq. 5 as function of the adiabatic index  $\gamma$ .

	$c_0$	$c_1$	$c_2$
Value	$\frac{\gamma-1}{2(2\gamma-1)}$	$\frac{3}{2}(\gamma+1)^2$	$3 + \frac{4\gamma}{\gamma+1}$
Value ( $\gamma = 5/3$ )	1/7	32/3	11/2

described by the following set of equations

$$\dot{M} \equiv \dot{M}_{\text{in}} + \dot{M}_{\text{sw}} = \dot{M}_{\text{in}} + \rho_0 \boldsymbol{\Sigma} \cdot \mathbf{v}_s, \quad (1)$$

$$\frac{d}{dt}(M\mathbf{v}_s) = \Delta P \boldsymbol{\Sigma} + M(\mathbf{g} - \dot{\mathbf{v}}_{\text{ext}}) + \dot{p}_{\text{in}} \mathbf{n}, \quad (2)$$

$$\dot{E} = \dot{E}_{\text{in}} - \dot{E}_{\text{cool}} + M\mathbf{g} \cdot \mathbf{v}_s, \quad (3)$$

$$\dot{\mathbf{r}}_s = \mathbf{v}_s + \mathbf{v}_{\text{ext}}, \quad (4)$$

where  $\dot{M}_{\text{in}}$ ,  $\dot{E}_{\text{in}}$  and  $\dot{p}_{\text{in}}$  are the central mass-, energy- and momentum-injection rates,  $\dot{M}_{\text{sw}}$  is the incorporation rate of swept-up mass,  $\dot{E}_{\text{cool}}$  is the energy dissipation rate due to radiative cooling  $\boldsymbol{\Sigma} = d\mathbf{A}/d\Omega$  is the (outward-) oriented surface area and  $\mathbf{n} = \boldsymbol{\Sigma}/\|\boldsymbol{\Sigma}\|$  is the outward-pointing normal vector of the shell-surface.

In the sector approximation, volumetric quantities such as energy, mass, and momentum are to be understood per unit solid-angle (i.e.,  $E = dE/d\Omega$ , etc.). For brevity of notation we omit this distinction, except where it could lead to confusion.

We evaluated the pressure gradient force  $\mathbf{F}_{\Delta P} = \Delta P \boldsymbol{\Sigma}$  using the formalism of Laumbach & Probst (1969) which lead to the expression

$$\Delta P = c_0 \left[ c_1 \frac{E}{3\delta V} + 3\rho_0 v_s^2 + (k_\rho - c_2) \frac{M v_s^2}{3\delta V} \right], \quad (5)$$

where we list the constants  $c_i$  in Tab. 1,

$$k_\rho = -\frac{d \log \rho_0}{d \log r_s}, \quad (6)$$

and we substituted  $r_s^3 \rightarrow 3\delta V$  to account for more general geometry. Due to the gauge freedom of  $\delta V$  described below this expression is ill-defined, but since the shock surface is usually spherical in the situations where it is relevant and thus  $\delta V \sim r_s^3/3$  this is only a minor concern. We direct the interested reader to the App. A for a derivation of Eq. 5. Radiative blastwaves are usually modeled by setting the adiabatic index  $\gamma = 1$ , which leads to  $\Delta P \propto (\gamma - 1) = 0$ . We thus set  $\Delta P = 0$  once radiative cooling becomes dominant.

The central mass-, energy- and momentum-injection rates are linked

$$\dot{p}_{\text{in}} = \alpha_p \sqrt{2\dot{M}_{\text{in}}\dot{E}_{\text{in}}}, \quad (7)$$

where  $\alpha_p$  is a boost-factor that accounts for the coupling of the interior of the SNR to the shell. For adiabatic blastwaves, this coupling is explicitly accounted for with the pressure gradient force Eq. 5 and we can set  $\alpha_p = 1$ , however Lancaster et al. (2024) have shown that radiative, continuously powered blastwaves approach a so-called rapidly-cooling wind solution, where the momentum injected into the shell is mediated by the hot interior, leading to slightly boosted momentum-injection with  $\alpha_p \sim 4$ .

The energy dissipation rate due to radiative cooling is

$$\dot{E}_{\text{cool}} = \chi \frac{\Lambda}{\mu^2} \rho_0 M, \quad (8)$$

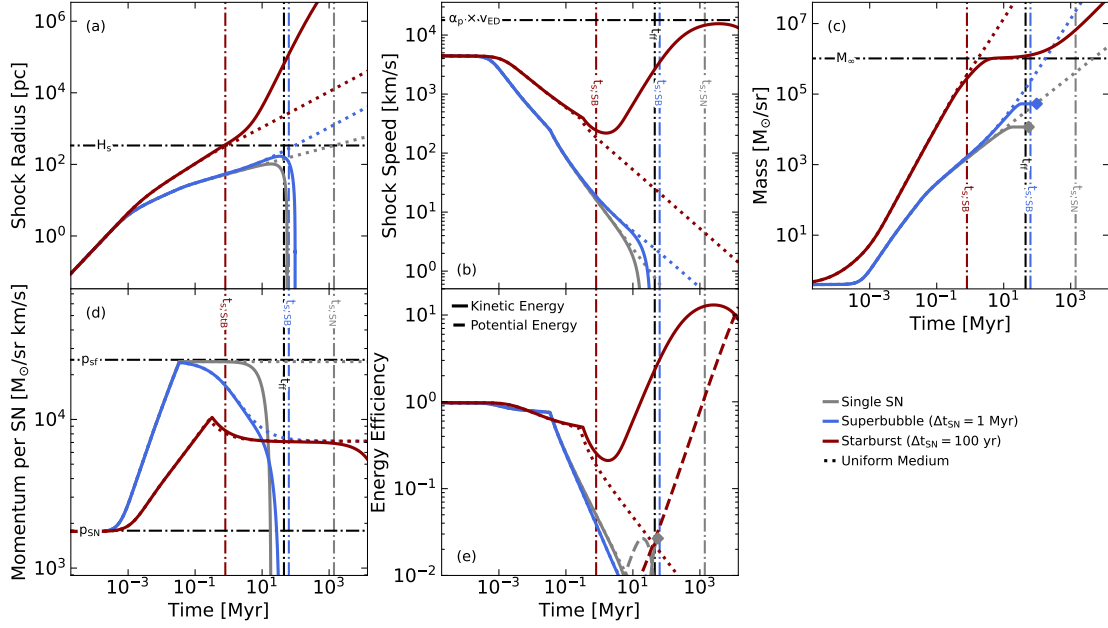


**Fig. 1.** Time evolution of shock radius (a), shock speed (b), swept-up mass (c), momentum per SN (d), and energy efficiency (e) in the case of blastwaves expanding into a vertically stratified atmosphere. For comparison, dotted lines corresponding to the same models expanding into a uniform medium are shown. Dash-dotted lines depict various characteristic scales. Both the single SN and the SB stall without breaking out of the galactic disk within about a free-fall timescale, due to the effect of gravity. Only the starburst can resist the gravitational field of the disk and drive a galactic wind.

where  $\chi = (\gamma + 1) / (\gamma - 1)$  is the shock-compression ratio in the case of a strong shock and  $\mu = 1.4 m_{\text{H}}$  is the mean atomic weight. We followed Oku et al. (2022) in approximating the cooling rate of an adiabatic blastwave as  $\Lambda = 10^{-22} \Lambda_{6,-22} T_{s,6}^{-0.7} \text{ erg s}^{-1} \text{ cm}^3$ , where  $T_s = 10^6 T_{s,6} \text{ K} = \tau \mu v_s^2 / k_{\text{B}}$  is the post-shock temperature and  $\tau = 2(\gamma - 1)(\gamma + 1)^{-2}$ .

We transitioned to the radiative stage by switching off cooling and pressure gradient forces and setting  $\alpha_p = 4$  once  $\geq 10\%$  of the thus far injected energy have been radiated away.

In contrast to previous work (e.g. Palouš et al. 2020), we do not modify the dynamics once the shock velocity falls below the velocity dispersion of the ambient medium or the internal pressure falls below the ambient pressure, since simulations do not show any signs of modified dynamics past this point (Romano et al. 2024, 2025a).

The surface area and its direction depend on the instantaneous geometry of the shock-surface, which either requires evolving the whole surface or a local parameterization of it in a neighborhood of each point—here we opted for the latter. The surface element is the vector product tangent vectors

$$\mathbf{\Sigma}(t) = \mathbf{\partial}_\theta \times \mathbf{\partial}_\phi, \quad (9)$$

$$\mathbf{\partial}_\theta = \frac{\partial \mathbf{r}_s}{\partial \theta}, \quad \mathbf{\partial}_\phi = \frac{1}{\sin(\theta)} \frac{\partial \mathbf{r}_s}{\partial \phi}, \quad (10)$$

which are known at  $t = 0$  and where we divided out the constant  $\sin(\theta)$  for regularity near the poles<sup>2</sup>. We describe their dynamical evolution in the Appendix B.

Finally, we defined<sup>3</sup> the local volume-element as

$$\delta V = \frac{1}{3} (\mathbf{r}_s - \mathbf{r}_{\text{expl}}) \cdot \mathbf{\Sigma}, \quad (11)$$

<sup>2</sup> This factor only enters in surface-integrals where now  $\Delta\Omega = \sin(\theta) \Delta\theta \Delta\phi$ .

<sup>3</sup> There is some freedom in the definition of the local volume element. For instance, by applying the divergence theorem the dot-product of any function  $\mathbf{F}$  with  $\text{div } \mathbf{F} = 1$  with  $\mathbf{\Sigma}$  defines a viable volume-element.

where we allowed the explosion center  $\mathbf{r}_{\text{expl}}(t)$  to move as a function of time to model cases where it is not stationary, such as a star cluster following a circular orbit in a galactic disk.

We confirm both analytically and numerically that FRANZ reproduces the well established behavior of blastwaves in uniform media in the Appendix C.

## 2.1. Initial Conditions

FRANZ is general enough to describe a variety of different types of blastwaves, such as SNe, stellar winds and active galactic nuclei, which may require different initial conditions as well as models for their environment. Here we focused on SN-driven SBs, which begin to expand following a central point-explosion that deposits a large amount of energy  $E_0$  and mass  $M_0$  at  $t = 0$ . Due to the initial spherical symmetry  $\mathbf{\Sigma} = r_s^2 \hat{\mathbf{e}}$ , where  $r_s$  is the shock radius. Regularity of the solution at  $r_s = 0$  requires the terms in  $\Delta P r_s^2$  that are  $\propto r_s^{-1}$  to cancel as  $r_s \rightarrow 0$ , which leads to  $(r_s, v, M, E) = (0, \sqrt{cE_0/M_0}, M_0, E_0)$ , where  $c = c_1 / (c_2 - k_p)$ .

Despite this cancellation, we started our calculation from a slightly advanced state with  $r_s \geq 0$  to avoid numerical problems due to division by zero.

## 2.2. Breakdown of the model

While FRANZ is applicable under a wide range of conditions, there are regimes in which it ceases to yield physically meaningful results. Below we summarize common causes of breakdown and their physical interpretation.

In models with gravity, the shock expansion may reverse and lead to collapse. In this situation, where  $\mathbf{v}_s \cdot \mathbf{\Sigma} < 0$ , physically we expect the shock to stop sweeping up mass. To prevent a for-

The equivalence class of volume-elements corresponds to such functions differing only by a total derivative on the shock surface.

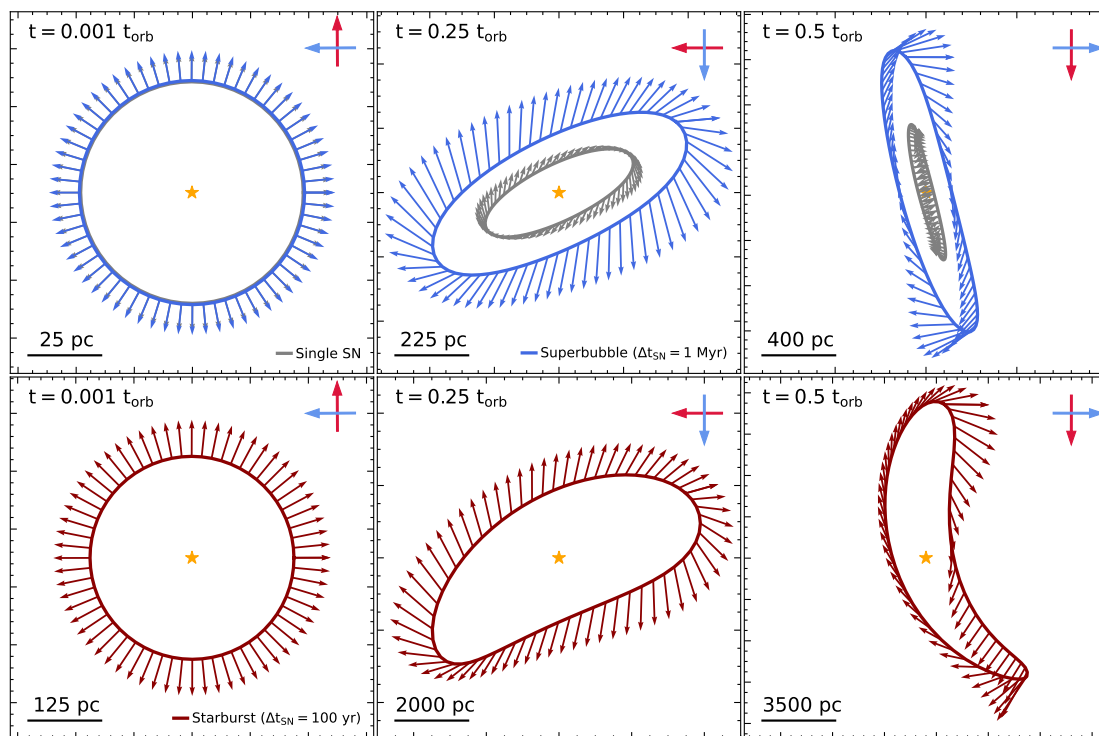


**Fig. 2.** Slices through the  $xy$ -plane of the shock-surface of different blastwave models expanding in a shearing, uniform density medium ( $n_0 = 1$ ,  $R_3 = 8$ ,  $V_{\text{rot}, 2} = 2$ ). The velocity vectors on the surface are shown as arrows with arbitrary scaling. Top panels show the single SN and SB models; bottom panels show the starburst. Left, center and right panels show slices after 0.1 %, 1/4 and 1/2 of an orbit, respectively. Each panel has a compass pointing towards the galactic center (blue) and the direction of rotation (red). While the SNRs are initially spherically symmetric, after  $t_{\text{orb}}/4$  they are significantly stretched out with a pitch angle  $\sim 30^\circ$ . The velocity vectors clearly show signs of the epicyclic motion described by Eqs. 31 - 32. After  $\sim t_{\text{orb}}/2$  they cease to be star-shaped making it difficult to measure their geometric properties with our methods.

mal breakdown of the model, we thus set  $\dot{M}_{\text{sw}} = 0$ . If the shock subsequently re-expands, care must be taken to avoid double-counting material that may have been swept up previously.

Provided the surface normal initially points outward, the topology ensures that it remains outward-facing unless it undergoes a continuous transition to an inward orientation, which requires passing through a singular point with  $\|\Sigma\| = 0$ . Using Eq. B.1, the time evolution of the surface normal is given by

$$\frac{d}{dt}\Sigma = (\nabla \cdot \dot{\mathbf{r}}_s - (\nabla \dot{\mathbf{r}}_s)^T)\Sigma, \quad (12)$$

which shows that converging flows within the tangent plane of the shock can drive  $\Sigma$  to zero. We thus interpret this singularity as the crossing of neighboring streamlines. Beyond this point the local description is no longer valid. Physically, such behavior may correspond to strong compression, or even collapse, of swept-up material and it may therefore be of astrophysical interest to identify where this behavior occurs.

Finally, in certain setups—such as an adiabatic shock expanding into a medium of finite mass—the shock velocity can diverge in finite time (Laumbach & Probst 1969; Koo & McKee 1990). The appearance of such divergent or otherwise unphysical behavior signals the breakdown of one or more underlying assumptions, such as neglected physics (e.g., radiative cooling or gravity) or an idealized environment, and must be addressed on a case-by-case basis.

### 3. Application: SNRs in SISSI

We used FRANZ to quantify how a realistic galactic environment can affect the properties of SNRs. We particularly focused

on ages  $\gtrsim 1$  Myr, where our numerical simulations have begun to deviate from previous analytical models (RBB25). We considered three different explosion models—all with radiative cooling:

1. A single SN explosion (SN).
2. An SB powered by 1 SN every  $\Delta t_{\text{SN}} = 1$  Myr (SB).
3. A starburst powered by 1 SN every  $\Delta t_{\text{SN}} = 100$  yr (StB).

Each SN injects a total energy of  $E = 10^{51} E_{51}$  erg and a mass of  $M_{\text{ej}} = M_{\text{ej}, 0} M_\odot$ , corresponding to a momentum of  $p_{\text{SN}} \sim 10^4 p_4 M_\odot \text{ km s}^{-1}$  across the whole sky. For convenience we write  $\Delta t_6 = \Delta t_{\text{SN}}/\text{Myr}$  and  $\dot{p}_{\text{in}} = 10^4 \dot{p}_4 M_\odot \text{ km s}^{-1} \text{ Myr}^{-1}$ .

For the environmental effects that might affect SNR evolution we considered vertical stratification, galactic rotation and the effect of dense substructures. To obtain an intuition for each, we first considered each effect separately, before discussing their combined effect in concert.

#### 3.1. Vertical stratification

While the theory of adiabatic blastwaves expanding into a stratified atmosphere is well established, most astrophysical blastwaves are expected to cool long before they can be affected by vertical stratification. Moreover, blastwaves breaking out of the galactic disk are subject to the galaxy's gravitational pull, which can keep shocks from leaving the galactic ecosystem (Romano et al. 2025b). However, so far these effects have received only little attention (Bisnovatyi-Kogan & Silich 1995; Orr et al. 2022; Jiménez et al. 2024).

To address this gap, we applied FRANZ to the vertical expansion of a blastwave from the midplane of an isothermal slab

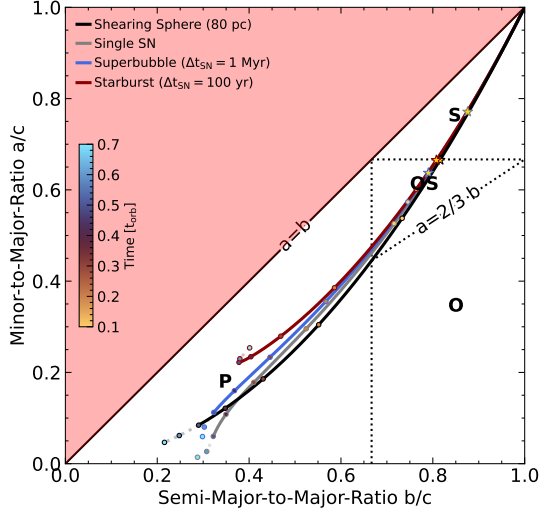


**Fig. 3.** Evolutionary tracks in the shape phase-space of the blastwave models expanding in a shearing, uniform density medium ( $n_0 = 1$ ,  $R_3 = 8$ ,  $V_{\text{rot},2} = 2$ ). In different parts of the phase space the SNRs are either spherical (S), oblate spheroids (OS), prolate (P) or oblate (O). The track of a shearing sphere with a constant radius of 80 pc is shown in black. The time at which the blastwaves are expected to cross the  $a/c = 2/3$ -line is shown as star markers. We also plot circle-markers color-coded with the time to provide a reference how long it takes to reach a given degree of deformation. The blastwaves starts out as perfect spheres and become increasingly prolate over time. The blastwave models roughly follow the shearing sphere’s track, with a slight tendency of more powerful blastwaves towards larger  $a/b$ . After  $t_{\text{orb}}/2$  the measured lengths become increasingly unreliable and are thus shown as transparent, dotted lines.

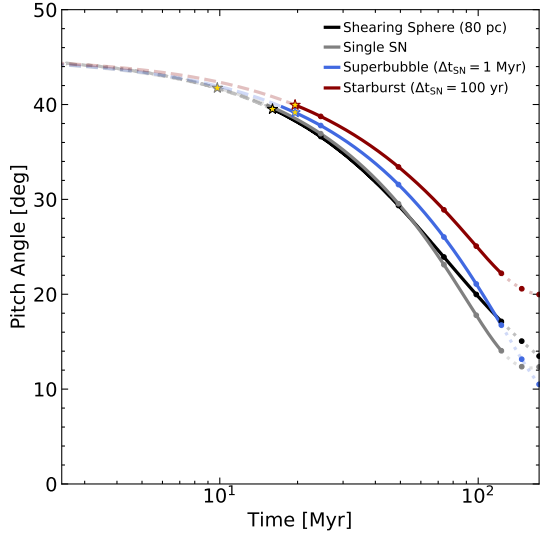


**Fig. 4.** Time evolution of the pitch angle of the major axis of the blastwave models expanding in a shearing, uniform density medium ( $n_0 = 1$ ,  $R_3 = 8$ ,  $V_{\text{rot},2} = 2$ ). For reference the pitch-angle of a shearing sphere with a constant radius of 80 pc is shown in black. The time at which the blastwaves are expected to cross the  $a/c = 2/3$ -line is shown as star markers. During the spherical phase ( $a/c > 2/3$ ) the pitch angle is not very meaningful and is thus shown as transparent dashed lines. After  $t_{\text{orb}}/2$  the measured angles become increasingly unreliable and are thus shown as transparent, dotted lines. The pitch angle starts off near  $45^\circ$  and decays over time. The blastwaves roughly follow the pitch-angle evolution of the shearing sphere with a tendency towards larger pitch angles for more rapidly expanding models.

in vertical hydrostatic-equilibrium. The density profile and gravitational acceleration are given by

$$\rho_0(z) = \rho_{\text{mp}} \cosh^{-2}\left(\frac{z}{H_s}\right), \quad (13)$$

$$g_z(z) = -2\frac{\sigma^2}{H_s} \tanh\left(\frac{z}{H_s}\right), \quad (14)$$

where

$$H_s = \frac{\sigma}{\sqrt{2\pi G \rho_{\text{mp}}}} \sim 338 \sigma_1 n_0^{-0.5} \text{ pc} \quad (15)$$

is the vertical scale height,  $\sigma = 10 \sigma_1 \text{ km s}^{-1}$  is the velocity dispersion of the ISM and  $\rho_{\text{mp}} = \mu n_0 \text{ cm}^{-3}$  is the midplane gas density. In this setup the mass that can be swept up by a blastwave approaches a finite value

$$\begin{aligned} M_\infty &= \int_0^\infty \rho_0(z) z^2 dz \\ &= \frac{\pi^2}{12} \rho_{\text{mp}} H_s^3 \sim 10^6 \sigma_1^3 n_0^{-1/2} M_\odot. \end{aligned} \quad (16)$$

We expect the dynamics to be strongly affected after a about a free-fall timescale

$$t_{\text{ff}} = \sqrt{\frac{3\pi}{32G\rho}} \sim 44.9 n_0^{-0.5} \text{ Myr}, \quad (17)$$

or after the blastwaves break out of the disk after

$$t_s \sim 1.4 \sigma_1^4 n_0^{-0.87} E_{51}^{-0.93} \text{ Gyr} \quad (\Delta t_{\text{SN}} \rightarrow \infty), \quad (18)$$

$$t_s \sim 294 \sigma_1^2 n_0^{-0.5} \dot{\rho}_4^{-0.5} \text{ Myr} \quad (\Delta t_{\text{SN}} \ll t_s), \quad (19)$$

whichever occurs first.

We show in Figure 1 the dynamical evolution of the shock radius, the shock speed, the swept-up mass, the momentum per SN and the kinetic- and potential energy efficiencies per unit injected energy for the part of different blastwave models expanding vertically into a stratified medium with finite mass. The single SN and the SB model do not manage to break out from the midplane, due its strong gravitational pull, which starts to significantly affect the expansion momentum and speed after  $\sim 1/4 t_{\text{ff}}$ . The blastwaves stall after  $\sim 1/2 t_{\text{ff}}$  and  $\sim t_{\text{ff}}$ , in the SN and the SB cases, respectively, followed by fall-back onto the disk, leading to an increase in kinetic energy by converting the potential energy that was spent trying to escape the galactic potential. By contrast, The starburst model is powerful enough to overcome the gravitational potential and drive a galactic wind. After breaking out of the disk, the mass encountered by the shock is negligible, while the momentum keeps growing at a constant rate, leading to a constant acceleration. However, after  $\sim 200 \text{ Myr}$  the mass injected at the source, becomes comparable to the swept-up mass, and the gravitational force  $\propto M$  begins to grow and overpower the constant force of the central starburst. We note however, that the assumptions of our model cease to be valid on these vast spatial and temporal scales. Romano et al. (2025b) discuss the case of the starburst and its limitations in greater detail.

These results suggest that a blastwave will break out of the disk if  $t_s \ll t_{\text{ff}}$ , which leads to the condition

$$E_{51} \gg 40 \sigma_1^{4.3} n_0^{-0.4} \quad (\Delta t_{\text{SN}} \rightarrow \infty), \quad (20)$$

$$\frac{P_4}{\Delta t_6} \gg 43 \sigma_1^4 \quad (\Delta t_{\text{SN}} \ll t_s). \quad (21)$$

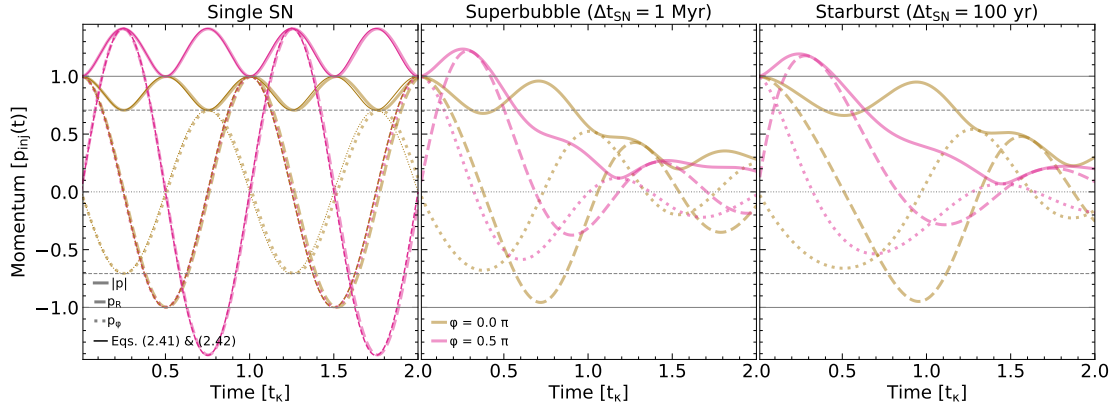


**Fig. 5.** Time evolution of the momentum components of blastwaves expanding in a shearing, uniform density medium ( $n_0 = 1$ ,  $R_3 = 8$ ,  $V_{\text{rot},2} = 2$ ). Different panels correspond to the different explosion models. Solid (dashed, dotted) lines correspond to the magnitude (radial-, azimuthal component) of the momentum vector. In the first panel, thin lines depict the expectation the analytical considerations matching well with the numerical results. Horizontal lines correspond to integer multiples of the radial momentum  $p_{\text{inj}}$  and  $p_{\text{inj}}/\sqrt{2}$  of a model without shear.

However, as shown by Romano et al. (2025b) even if a blastwave breaks out of the disk, unless it is powerful enough to escape the galaxy’s gravitational potential it will eventually fall back onto the disk. This might be interpreted as fountain flow.

These results highlight the importance of radiative cooling and gravity for the dynamics of blastwaves in stratified media. While we have neglected the change in the surface area element in our analytical derivation, we confirm that the deviations from  $\|\Sigma\| = r_s^2$  are negligible before the onset of collapse. Moreover, these results support the finding of RBB25 that the minor axis of the simulated blastwaves tends to be aligned with the galactic polar / vertical direction, especially for the SNRs in the densest regions, where the free-fall timescale is more comparable to the simulated 10 Myr.

We note however, that the simplistic picture of a uniform galactic midplane in vertical hydrostatic equilibrium lacks potentially relevant details, such as low-density channels carved out by turbulence and previous generations of feedback, through which weak SBs and even single SNe might be able to break out of the disk and contribute to the galactic fountain flow or galactic winds.

### 3.2. Galactic rotation

Observational evidence (Watkins et al. 2023) and theoretical studies (Bisnovaty-Kogan & Silich 1995; Jiménez et al. 2024) suggest that large SBs may be subject to galactic shear, which can stretch out their geometry along the rotation direction (Palouš et al. 2020). In the appendix of RBB25 we have presented a simple model for the deformation by galactic shear for the case of the so-called shearing sphere, a sphere of initially constant radius. According to this model, the volume of the structure is unaffected by the deformation, which becomes significant after  $\sim 5 - 6\%$  of an orbit, corresponding to a time of

$$t_{\text{deform}} \sim 0.065 t_{\text{orb}} \sim 4 R_3 V_{\text{rot},2}^{-1} \text{ Myr}, \quad (22)$$

similar to the timescale on which SNRs evolve. Here,  $R = R_3$  kpc is the galactocentric radius,  $V_{\text{rot}} = 100 V_{\text{rot},2}$  km s $^{-1}$  is the galactic rotation speed and  $t_{\text{orb}} = 2\pi R/V_{\text{rot}}$  is the orbital timescale.

However, in contrast to the deformation of a structure of fixed size, in the case of SNRs, the expanding motion may couple to the galactic rotation and affect the dynamics in non-trivial ways, that we explore in this section.

We consider blastwaves in a uniform density medium, subject to differential rotation of the form

$$\mathbf{v}_{\text{ext}} = V_{\text{rot}} \hat{\mathbf{e}}_{\varphi}(\varphi), \quad (23)$$

$$\mathbf{g} = -\frac{V_{\text{rot}}^2}{R} \hat{\mathbf{e}}_R(\varphi), \quad (24)$$

where  $\hat{\mathbf{e}}_{\varphi}$  and  $\hat{\mathbf{e}}_R$  are the local unit vectors pointing in the (galactic) azimuthal, and radial direction, respectively, and  $\varphi$  is the azimuthal angle. As the shell expands, its azimuthal angle changes, leading to an implicit time-dependence of  $\mathbf{v}_{\text{ext}}$  that enters into the equation-of-motion Eq. 2 through

$$\dot{\mathbf{v}}_{\text{ext}} = \frac{d\mathbf{v}_{\text{ext}}}{d\varphi} \dot{\varphi} = -\frac{V_{\text{rot}}(V_{\text{rot}} + v_{s,\varphi})}{R} \hat{\mathbf{e}}_R(\varphi), \quad (25)$$

where  $v_{s,\varphi}$  is the azimuthal component of the expansion velocity. For numerical evaluations we consider blastwaves exploding at  $R_3 = 8$ , in a medium with an ambient density of  $n_0 = 1$  and a rotation speed of  $V_{\text{rot},2} = 2$ .

In order to estimate the conditions under which SNRs are strongly affected by shear we consider its effect on the blastwave equation of motion Eq. 2. Since the timescale for shear to affect the dynamics of an SNR is usually much longer than the shell-formation timescale, here we consider the dynamics of a radiative blastwave under the influence of galactic shear. The equation of motions for the azimuthal and radial momentum components can be written as

$$\dot{v}_{s,\varphi} = -\frac{\dot{M}}{M} v_{s,\varphi} - \frac{V_{\text{rot}}}{R} v_{s,R} - \frac{v_{s,\varphi} v_{s,R}}{R} + \frac{\dot{p}_{\text{in},\varphi}}{M}, \quad (26)$$

$$\dot{v}_{s,R} = -\frac{\dot{M}}{M} v_{s,R} + 2 \frac{V_{\text{rot}}}{R} v_{s,\varphi} + \frac{v_{s,\varphi}^2}{R} + \frac{\dot{p}_{\text{in},R}}{M}, \quad (27)$$

where subscripts  $R$  and  $\varphi$  correspond to the (galactic) radial and azimuthal components, respectively.

Since the inertial term  $\propto \dot{M}/M$  is  $\propto v_s^2/r_s$  it decays faster than the terms  $\propto V_{\text{rot}} v_s/R$  as the expansion slows down. Thus, we expect galactic rotation to become dynamically important when the two terms become comparable, i.e. once  $v_s/r_s \sim V_{\text{rot}}/R$  at

$$t_{\text{shear}} \sim (8\pi)^{-1} t_{\text{orb}} \quad (\Delta t_{\text{SN}} \rightarrow \infty), \quad (28)$$

$$t_{\text{shear}} \sim (4\pi)^{-1} t_{\text{orb}} \quad (\Delta t_{\text{SN}} \ll t_{\text{shear}}), \quad (29)$$

which are both comparable to the deformation timescale of the shearing-sphere.

We illustrate the SNRs' morphological evolution through slices in the  $xy$ -plane shown in Fig. 2. Moreover, we provide a quantitative description in Figs. 3 and 4 showing the trajectories in the shape phase-space and the time evolution of the pitch angle, respectively. The shape phase-space tracks the minor-to-major ( $a/c$ ) and intermediate-to-major ( $b/c$ ) axis ratios, while the pitch angle measures the orientation of the shock surface relative to the galactic rotation vector, with  $90^\circ$  pointing toward the galactic center and  $-90^\circ$  toward the anti-center. We quantified the geometry of the blastwaves using the same ellipsoidal approximation outlined in RBB25 (see also App. D).

All SNRs evolve from an initially spherical shape towards increasingly prolate geometries, reaching pitch angles on the order of  $\sim 30^\circ$  by  $t_{\text{orb}}/4$ . In the single SN and SB models the geometry is quite similar suggesting that shear-induced motion dominates their evolution. By contrast, the starburst develops a more strongly curved geometry (higher  $a/b$ ). In all cases the geometry is well approximated by the shearing sphere, though more powerful SNRs have a tendency towards higher  $a/b$  and a slower decline of the pitch angle. After  $\sim t_{\text{orb}}/2$  the SNRs cease to be star-shaped, at which point the ellipsoidal approximation used to characterize their geometry becomes increasingly unreliable, as indicated by kinks in the shape phase-space trajectories.

Curiously, the velocity field exhibits a differential offset from pure expansion, resembling epicyclic motion. To understand the origin of this motion in the case of the single SN, we can drop the subdominant term  $\propto v_s^2/R$  (assuming  $r_s \ll R$ ) and assume  $R \sim \text{const.}$  to find a coupled harmonic (epicyclic) oscillation of the momenta, with an oscillation frequency of

$$\kappa = 2\sqrt{2}\pi t_{\text{orb}}^{-1}, \quad (30)$$

and an associated epicycle timescale  $t_\kappa = t_{\text{orb}}/\sqrt{2}$ . Due to the factor of 2 in the radial equation of motion the ratio of the amplitudes of the radial and the azimuthal momentum-oscillations is  $p_{s,R}^{\text{max}}/p_{s,\phi}^{\text{max}} = \sqrt{2}$ . In the case of consecutive SNe, the momentum injection will lead to deviations from this oscillation.

By assuming that at the onset of the oscillation, the direction of the motion in the co-rotating frame has hardly changed, we estimate the functional shape of the momentum oscillation by

$$p_{s,R}(t, \phi) \approx \sqrt{2} p_{s,\phi}^{\text{max}}(t, \phi) \cos(\kappa t - \phi), \quad (31)$$

$$p_{s,\phi}(t, \phi) \approx -p_{s,\phi}^{\text{max}}(t, \phi) \sin(\kappa t - \phi), \quad (32)$$

where  $\phi$  is the initial angle between the motion and the galactocentric radial direction, where the amplitude is given by momentum conservation at the onset of the oscillation

$$p_{s,\phi}^{\text{max}}(t, \phi) \approx \frac{p_{\text{sf}}}{\sqrt{1 + \cos^2(\phi)}}, \quad (33)$$

in particular  $p(t=0, \phi) = \sqrt{p_{s,R}^2 + p_{s,\phi}^2} = p_{\text{sf}}$  in the case of a single SN, while we expect the amplitude to grow accordingly in the case of continuous momentum injection.

We quantify these expectations over two epicycles in Fig. 5, where for each blastwave model, we track two representative points on the shock surface: one initially moving radially outward and one moving parallel to the galactic rotation. For a single SN, Eqs. 31 - 32 accurately capture the momentum evolution. The neglected term  $\propto v^2/R$  introduces only a small phase shift that accumulates over multiple epicycles. Galactic shear slightly enhances the momentum in initially azimuthal directions, while it slightly reduces the total momentum in initially radial directions. In contrast, models with consecutive SNe only briefly exhibit oscillatory behavior before the momentum decays. After

two epicycles, the continuously driven models retain only  $\sim 25\%$  of the injected momentum, indicating that the epicyclic response and the outward-directed injection counteract each other and reduce the overall efficiency of momentum coupling.

We summarize the evolution of the different blastwave models in Fig. 6. Despite transient momentum enhancement in azimuthal directions, we find that galactic rotation suppresses the overall expansion. In all models, after  $t_\kappa/4 \sim 40$  Myr the velocity starts to fall below that of the models without shear, while from  $t_\kappa/2 \sim 80$  Myr onward, the remnant size falls significantly below that of an equivalent model without shear. This matches with the expected decline and reversal of the net expansion speed and radial momentum. At the same time, the tangential momentum grows to values comparable to the initial blastwave momentum, leading to significant tangential motion, comparable to the expansion. In the case of the single SN the total kinetic energy grows larger than in the corresponding model without shear, while in the continuously driven models it falls below. This mechanism might play an important role for blastwave-driven turbulence generation.

### 3.3. Density structures

Many SNRs are observed to interact with dense structures in their environment (Hewitt & Yusef-Zadeh 2009; Mayker Chen et al. 2023; Watkins et al. 2023). Models and simulations have addressed such interactions of SNRs with their immediate surroundings (Haid et al. 2016; Makarenko et al. 2023; Lau & Bonnell 2025). Yet, models addressing the interaction of large SNRs with galactic scale structures, such as molecular filaments, spiral arms and massive clumps remain scarce.

We expect the sizes and separations of such structures to be on the order of the Jeans- and Toomre-lengths (Jeans 1902; Toomre 1964), which are approximately equal in a marginally stable disk (Toomre 1964),

$$\lambda_J = \left( \frac{15\sigma^2}{4\pi G\rho} \right)^{1/2} \sim 926 \sigma_1 n_0^{-1/2} \text{ pc}. \quad (34)$$

On scales comparable to  $\lambda_J$ , the gravitational acceleration towards such a structure is of order

$$g_J \sim \frac{\sigma^2}{\lambda_J} \sim \frac{\sigma}{t_{\text{ff}}}. \quad (35)$$

Slowly moving objects, with speeds  $v \lesssim \sigma$  – located within about a Jeans-length of the overdensity – experience free-fall onto it, reaching an asymptotic velocity of order  $\sigma$ .

In order to test how interactions with density structures may affect blastwave dynamics, we consider various setups featuring isothermal ‘‘Ostriker’’ filaments (Ostriker 1964) in an otherwise uniform background medium. The density profile and gravitational acceleration field of the filament are given by

$$\rho_{\text{fil}} = \frac{\rho_{\text{fil},0}}{\left(1 + (r/r_{\text{fil}})^2\right)^2}, \quad (36)$$

$$\mathbf{g}_{\text{fil}} = -4 \frac{\sigma_{\text{fil}}^2}{r_{\text{fil}}} \frac{\mathbf{r}/r_{\text{fil}}}{1 + (r/r_{\text{fil}})^2}, \quad (37)$$

where  $\mathbf{r}$  is the distance vector from the filament,  $r$  its length and

$$r_{\text{fil}} = 50 T_{\text{fil},2}^{0.5} n_{\text{fil},0}^{-0.5} \text{ pc} \quad (38)$$

is the filament's scale length, depending on its central density  $\rho_{\text{fil},0} = \mu n_{\text{fil},0} \text{ cm}^{-3}$  and its temperature  $T_{\text{fil}} = 100 T_{\text{fil},2} \text{ K}$ .

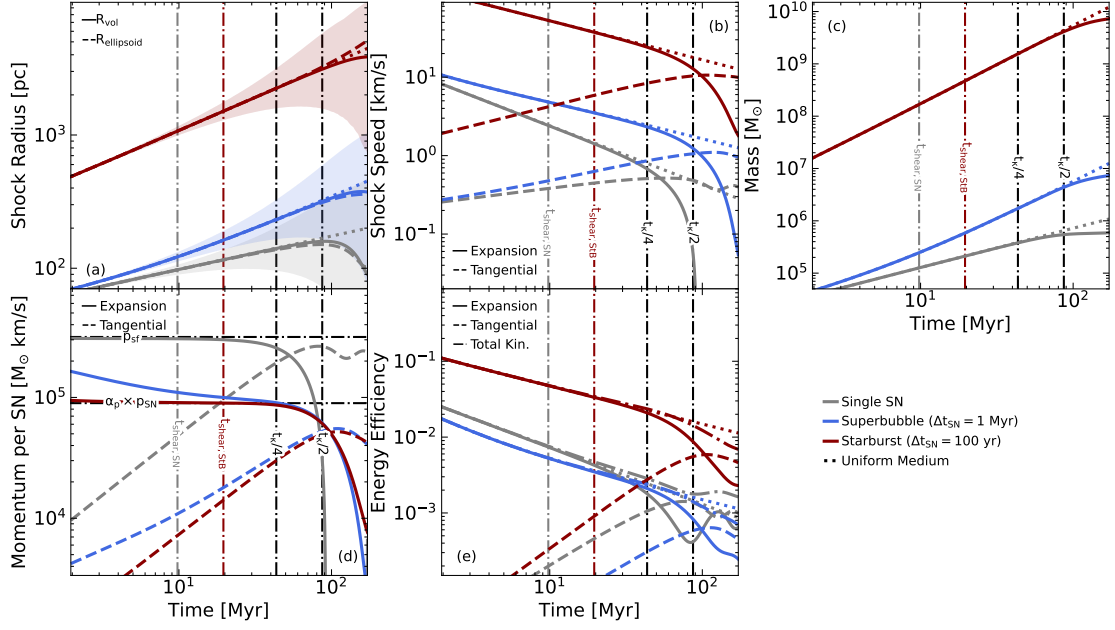


**Fig. 6.** Same as Fig. 1 for different blastwave models expanding in a shearing, uniform density medium ( $n_0 = 1$ ,  $R_3 = 8$ ,  $V_{\text{rot},2} = 2$ ). For comparison, dotted lines corresponding to the same models expanding into a uniform medium without shear are shown. Dash-dotted lines depict various characteristic scales. In all models the net expansion falls below that of the models without shear from  $\sim 80$  Myr, despite the epicyclic boost received in certain directions. Instead, a significant amount of the expansion momentum is converted into tangential motion.

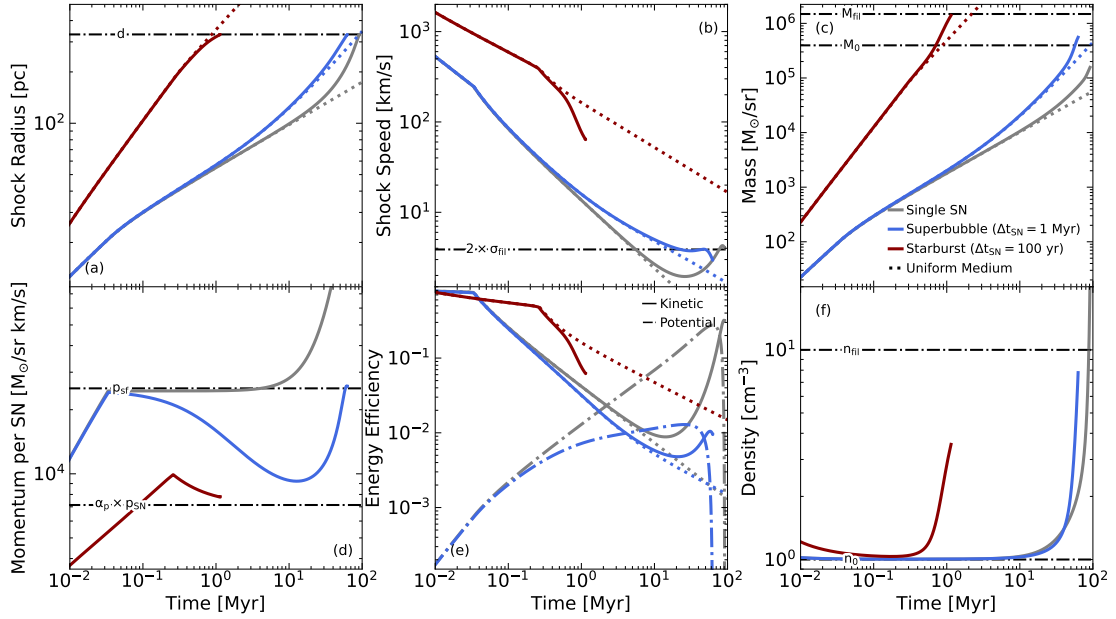


**Fig. 7.** Same as Fig. 1 for different blastwave models approaching a filament in a background medium ( $n_{\text{fil},0} = 10$ ,  $T_{\text{fil},2} = 6$ ,  $d = 8 \tau_{\text{fil}}$ ,  $n_0 = 1$ ). An additional panel (f) shows the average density to account for the environment's multi-phase nature. For comparison, dotted lines corresponding to the same models expanding into the unperturbed background medium are shown. Dash-dotted lines depict various characteristic scales. Both the single SN and the SB are trapped in the filament's gravitational potential, while the starburst can overrun it. In all cases the average density increases towards the filament's central density upon approach.

Evidently, if a blastwave occurs very far away from an overdensity, it will cover only a small solid angle on its surface and hardly affect its evolution, while a blastwave occurring within the overdensity can be effectively treated as expanding in a uniform density medium matching that of the overdensity—as long as it is smaller than the overdensity itself. We estimate the range, within which the overdensity contributes significantly to the blastwaves' dynamics by considering the ratio of the swept-up

mass attributable to the overdensity and the background, respectively:

$$\frac{M_0}{M_\delta} \sim \frac{d}{\delta \lambda_{J,\delta}}, \quad (39)$$

where  $\delta = n_{\text{fil}}/n_{\text{bg}}$  is the magnitude of the overdensity,  $d$  is the distance from the overdensity and  $\lambda_{J,\delta}$  its size. The impact of an overdensity in this range becomes immediately apparent, when

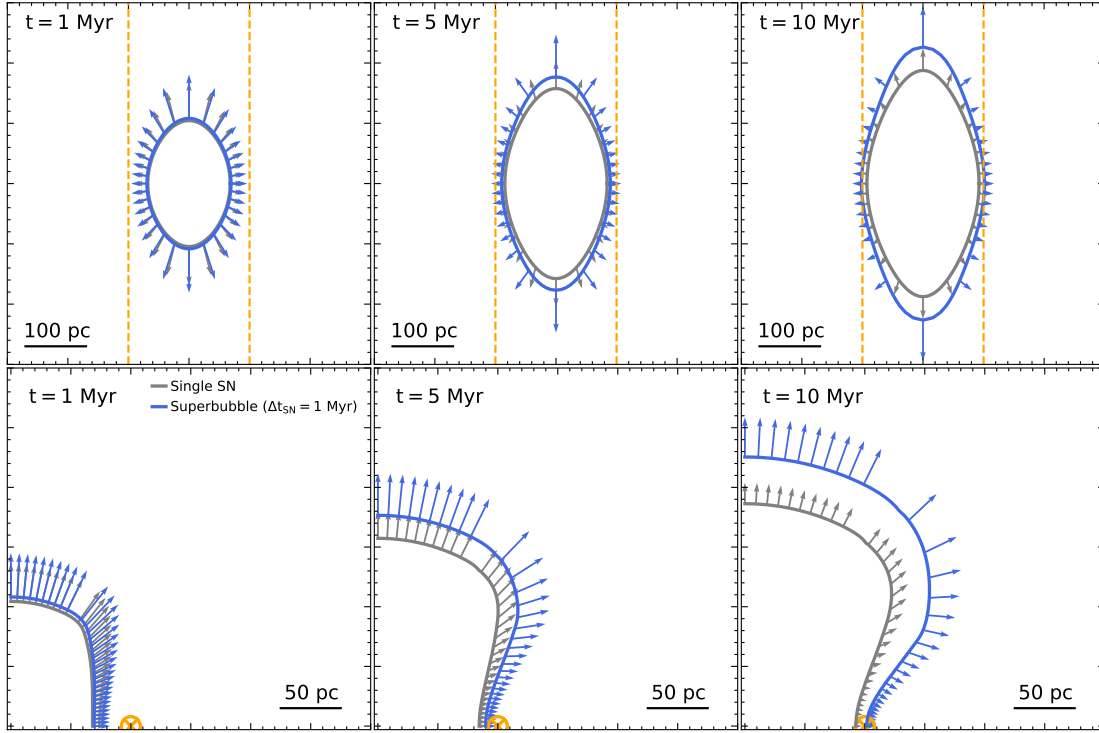


**Fig. 8.** Slices through the shock-surface of different blastwave models expanding into the gap ( $n_{\text{gap},0} = 0.1$ ) between two filaments ( $n_{\text{fil},0} = 10$ ,  $T_{\text{fil},2} = 2.65$ ,  $d_{\text{fil}} = 200$  pc). The velocity vectors on the surface are shown as arrows with arbitrary scaling. Top (bottom) panels show slices through the xy- (yz-) plane. Left, center and right panels show slices after 1, 5 and 10 Myr, respectively. Already at 1 Myr, the SNRs are quite deformed by the geometry of the ISM. The ratio between the SNRs' extent parallel to the filaments and towards them grows in time reaching axis ratios  $\sim 1/2$  by 5-10 Myr.

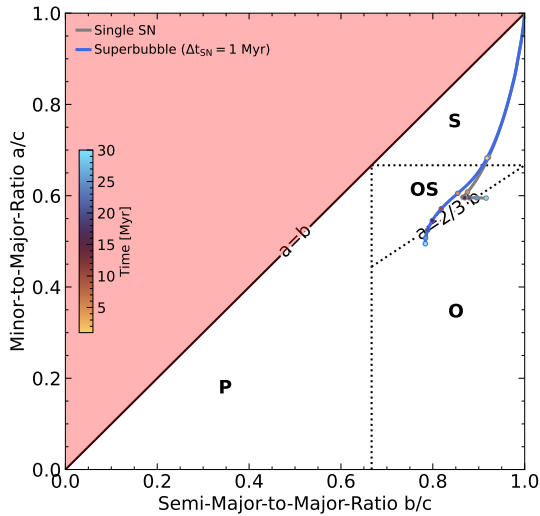


**Fig. 9.** Same as Fig. 3 for the different blastwave models expanding into the gap ( $n_{\text{gap},0} = 0.1$ ) between two filaments ( $n_{\text{fil},0} = 10$ ,  $T_{\text{fil},2} = 2.65$ ,  $d_{\text{fil}} = 200$  pc). The blastwaves starts out as perfect spheres and becomes increasingly deformed over time.

one considers radiative SNRs, where the expansion speed relative to that of an unperturbed SNR is suppressed by the above mass-ratio.

In order to explore the effect of an overdensity on the blastwaves' expansion, in Fig. 7 we show the evolution of blastwaves approaching a filament with a central density and temperature of  $n_{\text{fil},0} = 10$  and  $T_{\text{fil},2} = 6$  embedded in a constant density background with density  $n_0 = 1$ . The explosions occur at a distance

of  $d = 8 r_{\text{fil}} \sim 332$  pc away from the filament, where its contribution to the density amounts to only  $\sim 0.1\%$ . We stopped the calculation once the blastwave reaches the filament's center.

As expected the starburst overruns the filament. While its speed drops considerably upon reaching the overdensity, it remains well above the escape speed. By contrast, both the SB and the single SN get trapped in the gravitational potential and begin to free-fall approaching the asymptotic free-fall velocity of  $\sim 2 \sigma_{\text{fil}}$ . Compared to models without a filament, these models reach higher momentum and kinetic energy due to the filament's gravitational acceleration.

In all three models, the average density at the position of the filament exceeds that of the background medium. However, the final density differs between the models. The filament's gravitational field converges neighboring streamlines, leading to a contracting surface area element. While this in turn leads to a slower mass accretion it also shrinks the volume element, ultimately leading to a higher average density. In the case of the single SN the convergence of streamlines is so advanced that the density exceeds the filament's central density—a signature of gravitational collapse.

In order to study the net effect of galactic substructure on the geometry of blastwaves, we next consider blastwaves expanding in the gap between two parallel filaments—a setup that may naturally occur in galactic disks due to fragmentation and subsequent deformation by differential rotation. We place the filaments at a distance of 200 pc from each other, with a central density of  $n_{\text{fil},0} = 10$  and a temperature of  $T_{\text{fil},2} = 2.65$ , chosen such that the density in the gap is  $n_0 \sim 0.1$ , corresponding to an overdensity of  $\chi_{\text{fil}} = 100$ . The filaments are embedded in a uniform background

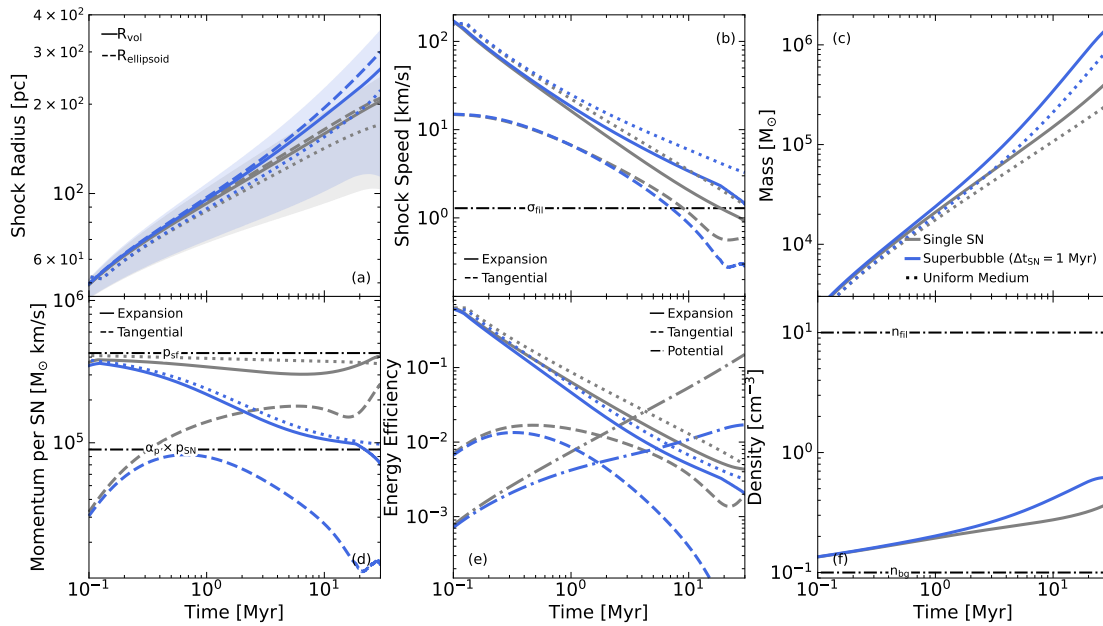


**Fig. 10.** Same as Fig. 7 for different blastwave models expanding into the gap ( $n_{\text{gap},0} = 0.1$ ) between two filaments ( $n_{\text{fil},0} = 10$ ,  $T_{\text{fil},2} = 2.65$ ,  $d_{\text{fil}} = 200$  pc). For comparison, dotted lines corresponding to the same models expanding into a uniform medium with an ambient density matching the average density of the corresponding inhomogeneous model at each point in time. Dash-dotted lines depict various characteristic scales. At the same average density, the blastwaves in inhomogeneous media grow larger than those in homogeneous media as indicated both by the radius panel (a) and the mass panel (c).

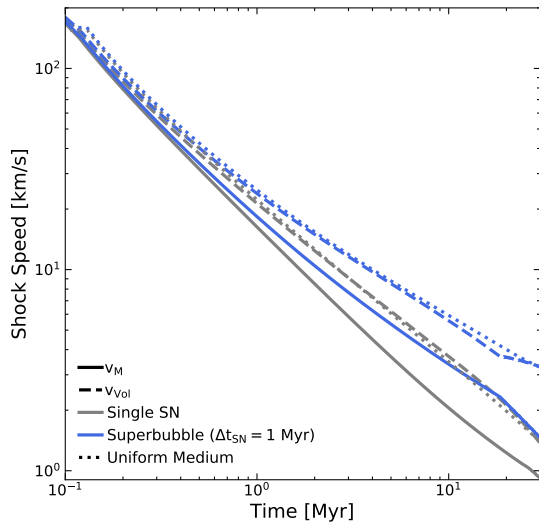


**Fig. 11.** Time evolution of the expansion velocity components of blastwaves expanding into the gap ( $n_{\text{gap},0} = 0.1$ ) between two filaments ( $n_{\text{fil},0} = 10$ ,  $T_{\text{fil},2} = 2.65$ ,  $d_{\text{fil}} = 200$  pc). Solid and dashed lines correspond to the mass-weighted expansion speed and the effective expansion speed obtained by computing the rate of change of the effective radius, respectively. For comparison, dotted lines correspond to the same models expanding into a uniform medium with an ambient density matching the average density of the corresponding inhomogeneous model at each point in time. The mass-weighted expansion speed is strongly suppressed due to the stalled expansion in the directions of the filaments, which contribute significantly to the total mass, but little to the total volume. The effective expansion speed roughly matches that of the uniform medium at the time-dependent average density.

medium with a density of  $n_0 = 0.1$ . We omit the starburst as it overruns the filaments before 1 Myr.

We illustrate the filaments' effect on the blastwaves' geometry by showing slices through the  $xy$ - and  $yz$ -planes in Fig. 8 after 1, 5 and 10 Myr of expansion. At a background density of  $n_0 \sim 0.1$  the blastwaves are expected to reach the filaments after  $\sim 1$  Myr and be significantly deformed after a few Myr. For the single-SN (SB) model, the minor-to-major axis ratio decreases to  $\lesssim 2/3$  ( $\sim 1/2$ ) after 5 Myr and evolves to  $\gtrsim 1/2$  ( $\sim 0.45$ ) after 10 Myr (see also the geometry tracks in Fig. 9). The portions of the shock surface expanding out of the midplane facing either filament are expanding in a low-density medium, but are pulled toward them, while the midplane region is stalled by the steep density gradient. This combination produces an increasingly concave, rectangular morphology, illustrating how galactic substructure can strongly shape the late-time geometry of SNRs and SBs.

This geometry differs from the geometry seen in the SISSI simulations (RBB25), where lower values of both  $a/c$  and  $b/c$  are obtained. These differences might arise from vertical stratification, more diversity in the galactic substructure and a deeper gravitational potential due to contributions from stars, all of which were neglected here for simplicity.

We summarize the evolution of the different blastwave models in Fig. 10. As expected the presence of the filaments increases the average density encountered by the SNRs. Despite the higher average density, the SNRs grow larger than they would in a uniform medium of the same average density. Curiously however, the mass-weighted expansion speed, obtained by dividing the momentum—which is only slightly affected by the presence of the filaments—by the mass is lower than the expansion speed in a uniform density medium. Moreover, the free-fall-driven acceleration that we found for the regions approaching the filaments in Fig. 7 is washed out, when considering the entire SNR. The presence of the filaments drives tangential motion, decaying from initially  $\sim 10$  km/s down to  $\lesssim \sigma_{\text{fil}}$  after  $\sim 10$  Myr which significantly contributes to the SNRs' momentum- and energy budget

in the case of a single explosion, but is rather negligible for the SB.

In order to make sense of the lower expansion speed despite the larger size, in Fig. 11 we compare the mass-weighted expansion speed  $v_M = p_{\text{exp}}/M$  to the effective expansion speed, defined as the rate of change of the effective radius  $v_{\text{vol}} = \dot{r}_{\text{vol}}$ . We find that the effective expansion speed roughly matches the expansion speed of a blastwave expanding in a uniform medium with ambient density matching the average density of the blastwave in an inhomogeneous medium. This motivates us to approximate the effective radius as

$$r_{\text{vol}}(t) \sim \int_0^t v_{\text{hom}}(t', \langle \rho(t') \rangle) dt', \quad (40)$$

as opposed to the usually applied

$$r_{\text{obs}}(t) \sim \int_0^t v_{\text{hom}}(t', \langle \rho(t) \rangle) dt', \quad (41)$$

where the difference lies only in the subtle fact, that the former expression requires information about the history of the average ambient density, while the latter depends only on the current “observable” density ( $\langle \rho(t') \rangle$  vs.  $\langle \rho(t) \rangle$ ). Since in our setup the density increases with time and a higher density implies a lower speed, this suggests that the “memory” of a previously encountered lower density medium automatically leads to a larger size compared to a model that expanded throughout with the higher average density at later times. Even for the slight overdensity considered here these effects become substantial after a few Myr. Observationally, it has been found that most SNe explode in diffuse gas Elwood et al. (2019). Thus this effect may provide a plausible explanation for the systematically larger radii at fixed average density reported by RBB25, and may have important consequences for observational age estimates of SBs that rely on blastwave-models in uniform, stationary media (Zucker et al. 2022; Romano & Burkert 2026).

### 3.4. Galactic environment in concert

The previous sections considered the effects of vertical stratification, galactic rotation and large-scale density structure in isolation. In realistic galaxies, however, these mechanisms operate simultaneously. In a marginally stable disk, many of the characteristic scales are linked through the Toomre parameter  $Q_T$  (Toomre 1964). The free-fall timescale is comparable to the epicyclic timescale, while the Jeans, Toomre and disk scale heights satisfy  $\lambda_J \sim \lambda_T \sim H_s$  (Jeans 1902; Toomre 1964; Ostriker 1964; Behrendt et al. 2015). Consequently, old remnants are expected to encounter several environmental effects at roughly the same evolutionary stage.

Our results suggest that environmental effects become important once remnants have expanded to scales of order  $\lambda_J$  and decelerated to velocities comparable to the ambient velocity dispersion,  $v_s \sim \sigma$ . Depending on the local environment, this transition occurs after a few Myr for interactions with nearby overdensities and after a few tens of Myr for vertical stratification and galactic shear. Modeling all of these processes simultaneously would require a time-dependent description of self-gravitating galactic substructure subject to differential rotation, approaching the complexity of full numerical simulations (RBB25).

Despite this complexity, several general trends emerge. Vertical stratification alone rarely leads to permanent breakout: only sufficiently powerful starbursts satisfy the conditions given by Eqs. 20 and 21 (Romano et al. 2025b), whereas weaker remnants

eventually stall and fall back as galactic fountain flows. At the same time, galactic shear and large-scale substructure jointly deform remnants into elongated, non-spherical morphologies. Because molecular clouds are themselves stretched by differential rotation, evolved SBs are expected to align preferentially with the surrounding filamentary ISM, producing pitch angles comparable to those observed for galactic filaments (Xie et al. 2024).

Finally, we have considered only the gravitational potential of the gas and stationary (or co-rotating) environments. In realistic galaxies, stellar and dark matter gravity, together with turbulent and anisotropic gas flows, are expected to introduce additional departures from the evolution in idealized uniform media, particularly once remnant velocities become comparable to the characteristic ISM velocity dispersion.

## 4. Limitations and future directions

FRANZ provides an efficient analytical framework for modeling blastwave evolution in arbitrary environments while remaining sufficiently simple to permit analytical insight. This makes it useful not only for rapid parameter studies but also for developing physical intuition. Nevertheless, the model has several important limitations.

The one-zone approximation precludes phenomena that depend on the internal structure of the remnant, including the evolution of the reverse shock (Truelove & McKee 1999), the pressure-driven snowplow phase (Haid et al. 2016), mixing across the contact discontinuity (Kim & Ostriker 2015; Guo et al. 2025), and blastwave implosion (Romano et al. 2024). Likewise, shell fragmentation by fluid instabilities (Vishniac 1994) cannot be captured directly, although the magnitude of the surface-normal may provide a useful diagnostic of shear-induced fragmentation. Future work is needed to validate this idea.

The fully local formulation based on the sector approximation enables arbitrary blastwave geometries at low computational cost, but neglects couplings between different parts of the shock surface that are included in existing models (e.g. Laumbach & Probst 1969; Tenorio-Tagle & Palous 1987; Bisnovatyi-Kogan & Silich 1995; Palouš et al. 2020; Jiménez et al. 2024). While future work is needed to assess the validity of this simplification, the successes showcased in this paper and the substantial improvements in terms of computational cost are encouraging.

At present, FRANZ includes hydrodynamics, gravity, radiative cooling and a simplified treatment of cosmic rays (Romano et al. 2025b). Its modular formulation and explicit representation of the local surface geometry make it straightforward to incorporate additional physics, such as magnetic fields, turbulence, multiphase gas, chemistry, dust, and a multi-zone descriptions that can resolve the dynamics blastwave interior and reverse shock.

Finally, the predicted evolution of the shock radius, velocity and swept-up mass can readily be coupled to secondary models of cosmic-ray acceleration (Cristofari et al. 2025), dust processing (Vasiliev 2025), chemistry and emission (Katsuragawa et al. 2022). FRANZ therefore provides a flexible framework for exploring blastwave evolution and connecting analytical models to observations.

## 5. Conclusions

In this paper we introduced FRANZ, a modular, analytical framework for one-zone blastwave dynamics that follows the evolution of the shock surface in arbitrary environments, offering great flexibility with explosion models. Building on the

thin-shell and sector approximations, the model extends classical analytical blastwave theory to complex galactic environments while remaining computationally inexpensive and easily extensible. Based on the model, we have published a code package written in Julia alongside this paper, which is publicly available from official Julia Registries and github.

We demonstrated that FRANZ reproduces a number of well-established theoretical limits in uniform media before applying it to quantify the effects of vertical stratification, galactic rotation and large-scale density structure on the evolution of SNRs. Our analysis lead to the following main conclusions:

1. Once gravity and radiative cooling are included, bertical stratification alone does not guarantee disk breakout. Single SNe and weak SBs stall after approximately one free-fall time before subsequently falling back toward the disk, whereas only sufficiently powerful SBs ( $\gg 40$  SNe within 1 Myr) are able to break out of the ISM.
2. Galactic shear becomes dynamically important after a quarter epicycle, a timescale that is much longer than the typical timescales for blastwave evolution in a typical galactic disk. SNRs are stretched into prolate shapes with pitch angles of  $\sim 15 - 45^\circ$ , undergo epicyclic momentum oscillations, that periodically convert between radial expansion and tangential motion. Epicyclic motion reduces the efficiency of momentum coupling in continuously driven blastwaves (Fig. 5), which might play a role in regulating feedback in galactic centers, where the shorter orbital timescales are comparable to feedback timescales.
3. Large-scale density structure strongly affects both the morphology and dynamics of SBs. Interactions with dense filaments produce highly anisotropic remnants and confound the observationally assigned ambient densities, affecting the interpretation of their expansion history. Ages assigned to SBs based on models in uniform media, may be systematically biased high.

The modular formulation of FRANZ makes it straightforward to incorporate additional physics, such as magnetic fields or cosmic rays. The framework provides a useful tool for identifying the physical mechanisms responsible for the observed morphology and dynamics of evolved SNRs and SBs, without the need of costly numerical simulations and may aid in the interpretation of observations in complex galactic environments as well as the development of improved subgrid prescriptions for stellar feedback in large-scale simulations.

*Acknowledgements.* Computations were performed on the scicomp system at the European Southern Observatory in Garching. This research was funded by the Deutsche Forschungsgemeinschaft (DFG, German Research Foundation) under Germany's Excellence Strategy – EXC 2094/2 – 390783311. I thank the developers of the following software and packages that were used in this work: JULIA v1.10.0 (Bezanson et al. 2017), MATPLOTLIB v3.3.2 (Hunter 2007), HEALPIX v4.2.4 (Tomasi & Li 2021), and FRANZ v0.1.0 (Romano 2026)

## References

Arias, M., Vink, J., de Gasperin, F., et al. 2018, A&A, 612, A110  
 Behrendt, M., Burkert, A., & Schartmann, M. 2015, MNRAS, 448, 1007  
 Bezanson, J., Edelman, A., Karpinski, S., & Shah, V. B. 2017, SIAM Review, 59, 65  
 Bisnovatyi-Kogan, G. S. & Silich, S. A. 1995, Reviews of Modern Physics, 67, 661  
 Breitschwerdt, D. & de Avillez, M. A. 2006, A&A, 452, L1  
 Breitschwerdt, D., Feige, J., Schulreich, M. M., et al. 2016, Nature, 532, 73  
 Cioffi, D. F., McKee, C. F., & Bertschinger, E. 1988, ApJ, 334, 252  
 Cristofari, P., Tatischeff, V., & Chabot, M. 2025, A&A, 693, A145

De Looze, I., Milisavljevic, D., Temim, T., et al. 2024, ApJ, 976, L4  
 Deng, Y., Zhang, Z.-Y., Zhou, P., et al. 2023, MNRAS, 518, 2320  
 Duffell, P. C., Polin, A., & Mandal, S. 2024, arXiv e-prints, arXiv:2403.13641  
 El-Badry, K., Ostriker, E. C., Kim, C.-G., Quataert, E., & Weisz, D. R. 2019, MNRAS, 490, 1961  
 Elwood, B. D., Murphy, J. W., & Díaz-Rodríguez, M. 2019, MNRAS, 483, 4551  
 Fierlinger, K. M., Burkert, A., Ntormousi, E., et al. 2016, MNRAS, 456, 710  
 Górski, K. M., Hivon, E., Banday, A. J., et al. 2005, ApJ, 622, 759  
 Guo, M., Kim, C.-G., & Stone, J. M. 2025, ApJ, 990, 49  
 Haid, S., Walch, S., Naab, T., et al. 2016, MNRAS, 460, 2962  
 Hewitt, J. W. & Yusef-Zadeh, F. 2009, ApJ, 694, L16  
 Hunter, J. D. 2007, Computing in Science & Engineering, 9, 90  
 Jeans, J. H. 1902, Philosophical Transactions of the Royal Society of London Series A, 199, 1  
 Jiménez, S., Silich, S., Mayya, Y. D., & Zaragoza-Cardiel, J. 2024, ApJ, 960, 81  
 Katsuragawa, M., Lee, S.-H., Odaka, H., et al. 2022, ApJ, 938, 23  
 Kim, C.-G. & Ostriker, E. C. 2015, ApJ, 802, 99  
 Kobashi, R., Lee, S.-H., Tanaka, T., & Maeda, K. 2024, ApJ, 961, 32  
 Kompaneets, A. S. 1960, Soviet Physics Doklady, 5, 46  
 Koo, B.-C. & McKee, C. F. 1990, ApJ, 354, 513  
 Lancaster, L., Ostriker, E. C., Kim, C.-G., Kim, J.-G., & Bryan, G. L. 2024, ApJ, 970, 18  
 Lau, C. S. C. & Bonnell, I. A. 2025, MNRAS, 540, 1124  
 Laumbach, D. D. & Probst, R. F. 1969, Journal of Fluid Mechanics, 35, 53  
 Makarenko, E. I., Walch, S., Clarke, S. D., et al. 2023, MNRAS, 523, 1421  
 Mayker Chen, N., Leroy, A. K., Lopez, L. A., et al. 2023, ApJ, 944, 110  
 Moellenhoff, C. 1976, A&A, 50, 105  
 Oku, Y., Tomida, K., Nagamine, K., Shimizu, I., & Cen, R. 2022, ApJS, 262, 9  
 Orr, M. E., Fielding, D. B., Hayward, C. C., & Burkhart, B. 2022, ApJ, 932, 88  
 Ostriker, J. 1964, ApJ, 140, 1056  
 Ostriker, J. P. & McKee, C. F. 1988, Reviews of Modern Physics, 60, 1  
 Palouš, J., Ehlerová, S., Wünsch, R., & Morris, M. R. 2020, A&A, 644, A72  
 Payli, G., Bakış, H., Aktekin, E., Sano, H., & Sezer, A. 2024, MNRAS, 527, 11685  
 Romano, L. E. C. 2026, leonardromano/Franz.jl: v0.1.0  
 Romano, L. E. C., Behrendt, M., & Burkert, A. 2024, ApJ, 965, 168  
 Romano, L. E. C., Behrendt, M., & Burkert, A. 2025a, A&A, 702, A12  
 Romano, L. E. C. & Burkert, A. 2026, A&A, 707, A98  
 Romano, L. E. C., Owen, E. R., & Nagamine, K. 2025b, A&A, 701, L5  
 Sedov, L. I. 1959, Similarity and Dimensional Methods in Mechanics (New York: Academic)  
 Slavin, J. D. & Cox, D. P. 1992, ApJ, 392, 131  
 Taylor, G. 1950, Proceedings of the Royal Society of London Series A, 201, 159  
 Tenorio-Tagle, G. & Palous, J. 1987, A&A, 186, 287  
 Tomasi, M. & Li, Z. 2021, Healpix.jl: Julia-only port of the HEALPix library  
 Toomre, A. 1964, ApJ, 139, 1217  
 Truelove, J. K. & McKee, C. F. 1999, ApJS, 120, 299  
 Vasiliev, E. O. 2025, arXiv e-prints, arXiv:2512.24677  
 Velázquez, P. F., Meyer, D. M. A., Chiotellis, A., et al. 2023, MNRAS, 519, 5358  
 Vishniac, E. T. 1994, ApJ, 428, 186  
 Watkins, E. J., Barnes, A. T., Henny, K., et al. 2023, ApJ, 944, L24  
 Weaver, R., McCray, R., Castor, J., Shapiro, P., & Moore, R. 1977, ApJ, 218, 377  
 Xie, Y.-H., Li, G.-X., & Chen, B.-Q. 2024, ApJ, 975, 39  
 Zhang, S., Tian, W., Zhang, M., Zhu, H., & Cui, X. 2023, ApJ, 942, 94  
 Zucker, C., Goodman, A. A., Alves, J., et al. 2022, Nature, 601, 334

## Appendix A: Derivation of the Pressure-Gradient Force

We derive the expression for the pressure-gradient force Eq. 5 following the formalism of Laumbach & Probst (1969). The expression for the pressure gradient can be read off from their final result, by noting that they consider an adiabatic blastwave, without central forcing, that expands into a stratified atmosphere, neglecting the effects of gravity. Under these assumptions the equation of motion Eq. 2 simplifies to

$$\frac{d}{dt}(Mv_s) = \Delta P r_s^2. \quad (\text{A.1})$$

The starting point of the derivation is the Taylor-expansion of the Eulerian radial coordinate  $r$  in terms of the Lagrangian radial coordinate  $r_0$  at  $t = 0$ , near the radial location of the shock front  $r_s$  to second order

$$r = r_s + \left. \frac{\partial r}{\partial r_0} \right|_{r_s} (r_0 - r_s) + \frac{1}{2} \left. \frac{\partial^2 r}{\partial r_0^2} \right|_{r_s} (r_0 - r_s)^2 + \dots \quad (\text{A.2})$$

In order to derive the equation of motion, we make use of the thin-shell approximation, in which  $r \rightarrow r_s$  is independent of  $r_0$ . In this approximation we can approximate the integral of the Euler-equation for the momentum evolution

$$\frac{\partial^2 r}{\partial t^2} = -\frac{r^2}{\rho r_0^2} \frac{\partial P}{\partial r_0}, \quad (\text{A.3})$$

using the value of the acceleration at the shock

$$\begin{aligned} P(0, t) - P_s(r_s) &= \int_0^{r_s} \frac{1}{r^2} \frac{\partial^2 r}{\partial t^2} \rho_0 r_0^2 dr \\ &\approx \frac{1}{r_s^2} \left. \frac{\partial^2 r}{\partial t^2} \right|_{r_s} M(r_s), \end{aligned} \quad (\text{A.4})$$

and similarly we can approximate the energy integral using the value of the kinetic energy density at the shock

$$\begin{aligned} E(r_s) &= \int_0^{r_s} \frac{P(r)}{\gamma - 1} r^2 dr + \int_0^{r_s} \frac{1}{2} \left( \frac{\partial r}{\partial t} \right)^2 \rho r_0^2 dr \\ &\approx \frac{P(0) r_s^3}{3(\gamma - 1)} + \frac{1}{2} M(r_s) \left( \frac{\partial r}{\partial t} \right)^2 \Big|_{r_s}. \end{aligned} \quad (\text{A.5})$$

By combining Eqs. A.4 and A.5 we can eliminate  $P(0, t)$ , which leaves us with the problem of deriving expressions for the various remaining quantities at the shock  $r_s$ .

### Appendix A.1: Derivation of the Acceleration at the Shock

To leading order(s) the first two time-derivatives of Eq. A.2 are

$$\begin{aligned} \left( \frac{\partial r}{\partial t} \right) &= \left( 1 - \left. \frac{\partial r}{\partial r_0} \right|_{r_s} \right) \dot{r}_s + \\ &+ \left[ \frac{\partial}{\partial t} \left( \left. \frac{\partial r}{\partial r_0} \right|_{r_s} \right) - \left. \frac{\partial^2 r}{\partial r_0^2} \right|_{r_s} \dot{r}_s \right] (r_0 - r_s) + \dots, \end{aligned} \quad (\text{A.6})$$

$$\begin{aligned} \left( \frac{\partial^2 r}{\partial t^2} \right) &= \left( 1 - \left. \frac{\partial r}{\partial r_0} \right|_{r_s} \right) \ddot{r}_s - \\ &- 2 \frac{\partial}{\partial t} \left( \left. \frac{\partial r}{\partial r_0} \right|_{r_s} \right) \dot{r}_s + \left. \frac{\partial^2 r}{\partial r_0^2} \right|_{r_s} \dot{r}_s^2 + \dots, \end{aligned} \quad (\text{A.7})$$

where  $\dot{r}_s = v_s$  is the shock speed.

The Eulerian and Lagrangian radial coordinates are related by the continuity equation

$$\rho_0 r_0^2 dr_0 = \rho r^2 dr, \quad (\text{A.8})$$

where  $\rho_0(r_0)$  is the unperturbed density profile at  $r_0$  and  $\rho(r, t)$  is the density at  $r$  and time  $t$ . We can use this relation in combination with the Rankine-Hugoniot jump-conditions for strong shocks (e.g. Ostriker & McKee 1988) to evaluate

$$\left. \frac{\partial r}{\partial r_0} \right|_{r_s} = \frac{\gamma - 1}{\gamma + 1} = \chi^{-1}, \quad (\text{A.9})$$

which is constant in time and determines the velocity at the shock

$$\left. \frac{\partial r}{\partial t} \right|_{r_s} = \frac{2}{\gamma + 1} v_s. \quad (\text{A.10})$$

By making use of the momentum equation A.3 and the Rankine-Hugoniot jump-condition for the pressure at the shock

$$P_s = \frac{2}{\gamma + 1} \rho_0(r_s) \dot{r}_s^2 \quad (\text{A.11})$$

we can evaluate Eq. A.7 at the shock to obtain

$$-\left. \frac{\partial^2 r}{\partial r_0^2} \right|_{r_s} \dot{r}_s^2 = \frac{2}{\gamma + 1} \dot{r}_s^2 \left( \left. \frac{1}{P} \frac{\partial P}{\partial r_0} \right|_{r_s} \right) + \frac{2}{\gamma + 1} \ddot{r}_s. \quad (\text{A.12})$$

The pressure-gradient term can be further evaluated by utilizing the adiabatic condition

$$\frac{P(r_0, t)}{P_s(r_0)} = \left( \frac{\rho(r_0, t)}{\rho_s(r_0)} \right)^\gamma, \quad (\text{A.13})$$

which yields for the pressure gradient at the shock

$$\left( \left. \frac{1}{P} \frac{\partial P}{\partial r_0} \right|_{r_s} \right) = \left( \frac{1}{P_s} \frac{\partial P_s}{\partial r_0} + \frac{\gamma}{\rho} \frac{\partial \rho}{\partial r_0} - \frac{\gamma}{\rho_0} \frac{\partial \rho_0}{\partial r_0} \right) \Big|_{r_s}. \quad (\text{A.14})$$

The first term can be evaluated from Eq. A.11 yielding

$$\left( \left. \frac{1}{P_s} \frac{\partial P_s}{\partial r_0} \right|_{r_s} \right) = \left( \frac{1}{\rho_0} \frac{\partial \rho_0}{\partial r_0} \right) \Big|_{r_s} + \frac{2\ddot{r}_s}{\dot{r}_s^2}, \quad (\text{A.15})$$

since by the chain-rule

$$\left( \left. \frac{\partial \dot{r}_s}{\partial r_0} \right|_{r_s} \right) = \ddot{r}_s \left( \left. \frac{\partial t}{\partial r_0} \right|_{r_s} \right) = \ddot{r}_s \dot{r}_s^{-1}. \quad (\text{A.16})$$

The second term can be evaluated using the continuity equation A.8 yielding

$$\left( \left. \frac{1}{\rho} \frac{\partial \rho}{\partial r_0} \right|_{r_s} \right) = \frac{1}{\rho_0} \left. \frac{\partial \rho_0}{\partial r_0} \right|_{r_s} + \frac{4}{\gamma + 1} r_s^{-1} - \chi \left. \frac{\partial^2 r}{\partial r_0^2} \right|_{r_s}. \quad (\text{A.17})$$

We thus obtain for the pressure gradient

$$\left( \left. \frac{1}{P} \frac{\partial P}{\partial r_0} \right|_{r_s} \right) = \left( \frac{1}{\rho_0} \frac{\partial \rho_0}{\partial r_0} \right) \Big|_{r_s} + \frac{2\ddot{r}_s}{\dot{r}_s^2} + \frac{4\gamma}{\gamma + 1} r_s^{-1} - \gamma \chi \left. \frac{\partial^2 r}{\partial r_0^2} \right|_{r_s}, \quad (\text{A.18})$$

which we can plug into Eq. A.12 and solve for  $\left( \left. \frac{\partial^2 r}{\partial r_0^2} \right|_{r_s} \right)$  to obtain

$$\left. \frac{\partial^2 r}{\partial r_0^2} \right|_{r_s} = -\frac{2\chi^{-1} k_p - 3 r_s \ddot{r}_s / \dot{r}_s^2 - 4\gamma / (\gamma + 1)}{r_s}. \quad (\text{A.19})$$

Finally, we can use this to obtain the acceleration at the shock

$$\left( \left. \frac{\partial^2 r}{\partial t^2} \right|_{r_s} \right) = \frac{4(2\gamma - 1)}{(\gamma + 1)^2} \ddot{r}_s - \frac{2\chi^{-1}}{\gamma + 1} \left( k_p - \frac{4\gamma}{\gamma + 1} \right) \frac{\dot{r}_s^2}{r_s}. \quad (\text{A.20})$$

## Appendix A.2: Obtaining the Equation of Motion

We have now all the pieces in place to derive the equation of motion. We combine Eqs. A.4 and A.5 to eliminate  $P(0, t)$ , plug in Eqs. A.11, A.10 and A.20 and solve for  $M\dot{v}_s$  to obtain

$$M\dot{v}_s = \frac{(\gamma + 1)^2}{4(2\gamma - 1)} \left[ 3(\gamma - 1) \frac{E}{r_s} - \frac{2}{\gamma + 1} \rho_0 r_s^2 v_s^2 + 2 \frac{\gamma - 1}{(\gamma + 1)^2} \left( k_\rho - \left( 3 + \frac{4\gamma}{\gamma + 1} \right) \right) \frac{M v_s^2}{r_s} \right], \quad (\text{A.21})$$

which by adding  $\dot{M}v_s = \rho_0 r_s^2 v_s^2$  finally yields the equation of motion

$$\frac{d}{dt} (Mv_s) = \frac{\gamma - 1}{2(2\gamma - 1)} \left[ \frac{3(\gamma + 1)^2}{2} \frac{E}{r_s^3} + 3\rho_0 v_s^2 + \left( k_\rho - \left( 3 + \frac{4\gamma}{\gamma + 1} \right) \right) \frac{M v_s^2}{r_s^3} \right] r_s^2, \quad (\text{A.22})$$

from which the expression for the pressure gradient Eq. 5 can be read off.

While this derivation assumes an adiabatic blastwave in a stationary medium, it might be possible to lift this assumption and derive the pressure-gradient force in more complex cases, such as a radiatively cooling isothermal shock. In this case the compression-ratio at the shock and the shock-pressure would need to be updated to those of an isothermal shock. Moreover, the adiabatic condition would need to be replaced with an appropriate equivalent condition, which might be challenging, and which is mainly the reason why we instead approximate the pressure-gradient force to become negligible once cooling becomes dominant. Future studies that do deal with this complication might be able to incorporate the role of cooling in this derivation and possibly recover the pressure-driven snowplow.

## Appendix B: Dynamical evolution of tangent vectors

We derive an equation of motion for the tangent vectors by switching the order of differentiation

$$\dot{\partial}_i = \partial_i \dot{r}_s = \partial_i v_s + \nabla v_{\text{ext}} \cdot \partial_i, \quad (\text{B.1})$$

where the external velocity gradient  $\nabla v_{\text{ext}}$  is known a priori, and  $\partial_i v_s$  is evolved along the flow making use of

$$\frac{d}{dt} \partial_i v_s = \partial_i \dot{v}_s(r_s, v_s), \quad (\text{B.2})$$

evaluated by approximating the local on-surface acceleration gradient using finite differences. In particular we evaluate the acceleration from eq. 2 by shifting the position, velocity and surface are element by the tiny increments

$$r_s \rightarrow r_s \pm \epsilon \partial_i \quad v_s \rightarrow v_s \pm \epsilon \partial_i v_s \quad \Sigma \rightarrow \Sigma \pm \epsilon \|\Sigma\| \hat{e}_i, \quad (\text{B.3})$$

where  $\hat{e}_i = \partial_i / \|\partial_i\|$ , and we approximated the local curvature radius with the length of the tangential vector for closure. We assume that all other quantities ( $M$ ,  $E$ , etc.) remain unchanged by a small shift along the surface and we choose  $\epsilon \sim 10^{-8}$  for it to be sufficiently small but not so small as to be dominated by numerical noise.

## Appendix C: Notable limits

We confirm that our model reproduces the behavior predicted by many previous studies in the appropriate limits. In Fig. C.1, we compare these limits to the results of numerically integrating Eq. 2 for spherically-symmetric blastwave expanding into a stationary, uniform ambient medium. We consider four different cases:

1. A single SN at  $t = 0$ , without radiative cooling.
2. A single SN at  $t = 0$ , with radiative cooling.
3. A single SN at  $t = 0$ , followed by continuous injection of energy and mass at a fixed rate, without radiative cooling.
4. A single SN at  $t = 0$ , followed by continuous injection of energy and mass at a fixed rate, with radiative cooling ( $\alpha_p = 4$ ).

Figure C.1 shows the temporal evolution of the shock-radius, shock-velocity, swept-up mass, momentum per SN, and the kinetic energy efficiency  $f_{\text{kin}} = E_{\text{kin}}/E_{\text{inj}}(t)$ . We recover all the limiting behavior highlighted below. Also highlighted are various characteristic timescales, such as the timescale for the transition from the ejecta-dominated to the adiabatic phase  $t_{\text{ED} \rightarrow \text{ST}}$  (Truelove & McKee 1999) and the shell-formation timescale  $t_{\text{sf}}$  (Cioffi et al. 1988; Kim & Ostriker 2015), which match the times at which the dynamics transition in our model quite well. The relatively high kinetic energy efficiencies ( $> 0.22 - 0.27$  (Sedov 1959; Weaver et al. 1977)) in the adiabatic cases are a well-known shortcoming of the thin-shell approximation (e.g. Koo & McKee 1990).

We note that in many cases, by changing the variable of integration from time to the radius, Eqs. 1 - 4 admit analytical solutions in terms of special functions. The resulting solutions are so-called unified solutions (Truelove & McKee 1999), which naturally interpolate between the limiting cases.

### Appendix C.1: Ejecta-dominated phase

Shortly after the central point-explosion, the SNR expands with an almost constant speed until the swept-up mass becomes comparable to the mass of the ejecta (Truelove & McKee 1999). In our model this behavior is recovered since for small radii  $r_s \ll (M/\rho_0)^{1/3}$  the acceleration is dominated by terms in  $\Delta P r_s^2$  that are  $\propto r_s^{-1}$ , i.e.

$$\dot{v}_s \sim \frac{c_0}{r_s} \left[ c_1 \frac{E}{M} + (k_\rho - c_2) v_s^2 \right], \quad (\text{C.1})$$

which rapidly drives  $v_s$  towards the constant speed  $v_{\text{ED}} = \sqrt{cE/M}$ , where  $c = c_1 / (c_2 - k_\rho)$ .

### Appendix C.2: Adiabatic phase

Once  $r_s \gtrsim (M/\rho_0)^{1/3}$  the contribution of the ram-pressure-terms in Eq. 2 can no longer be neglected. After a short transitional period the solution approaches a powerlaw solution resembling the Sedov-Taylor-solution  $r_s = \xi_{\text{ST}} (Et^2/\rho_0)^{1/5}$  (Sedov 1959) for a single explosion, or an energy-driven wind solution  $r_s = \xi_w (\dot{E}t^3/\rho_0)^{1/5}$  (Weaver et al. 1977) for continuous energy injection. We note that for a better comparison with the spherically symmetrical models of Sedov (1959) and Weaver et al. (1977) in these expressions  $E$  refers to the total energy deposited over the whole sky, i.e.  $E = \int (dE/d\Omega) d\Omega$ .

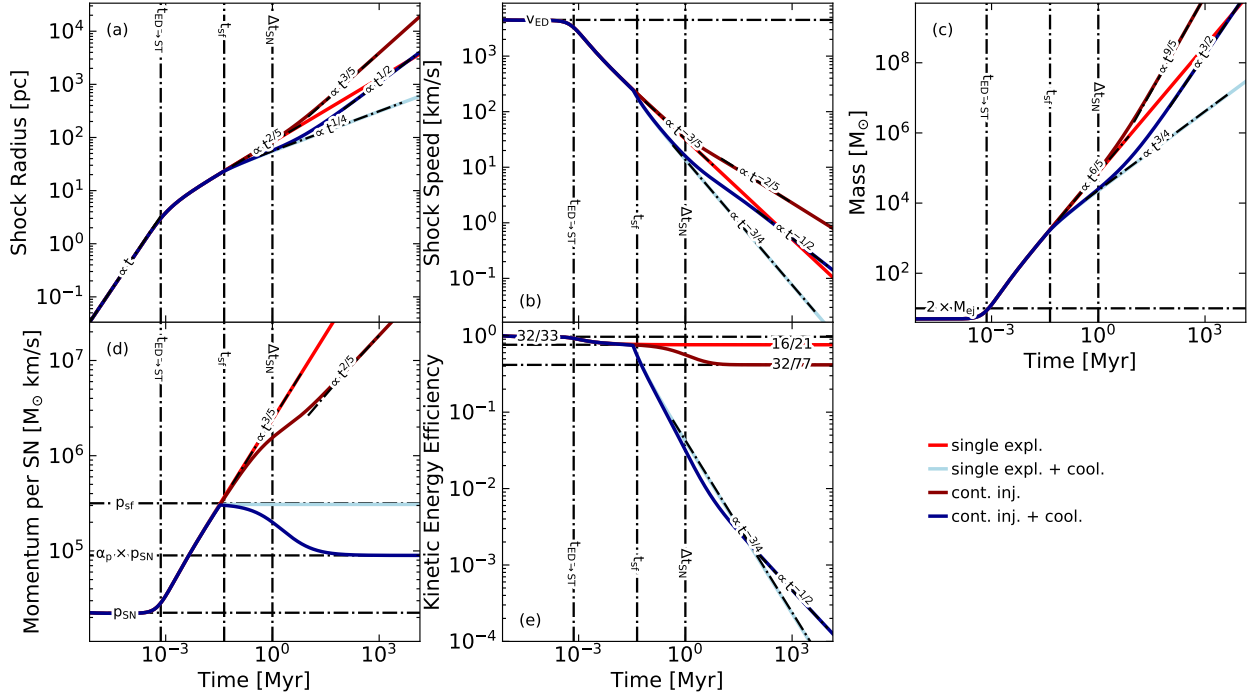


**Fig. C.1.** Same as Fig. 1 for different models in a stationary, uniform ambient medium. Black, dot-dashed lines denote characteristic scales or limiting behavior described in Appendices C.1-C.3.

By plugging the respective expressions for  $r_s(t)$  into Eq. 2 and solving for  $\xi$  we can find the asymptotic solution in the respective regime. For the Sedov blastwave ( $E = \text{const.}$ ) we find

$$\xi_{\text{ST}} = \left\{ \frac{25c_0c_1}{8\pi \left[ 1 - 2c_0 \left( 3 - (c_2 - k_p)/3 \right) \right]} \right\}^{1/5}, \quad (\text{C.2})$$

which for  $\gamma = 5/3$  and  $k_p = 0$  differs from the analytical solution only by  $\lesssim 2.34\%$ . For the continuously driven wind we obtain

$$\xi_{\text{W}} = \left\{ \frac{25c_0c_1}{4\pi \left[ 7 - 9c_0 \left( 3 - (c_2 - k_p)/3 \right) \right]} \right\}^{1/5}, \quad (\text{C.3})$$

which matches the solution found by Weaver et al. (1977) for  $\gamma = 5/3$  and  $k_p = 0$  with 1% accuracy.

### Appendix C.3: Radiative phase

In the absence of the pressure-gradient force and any external forces, the combined momentum of the blastwave and the ejecta is conserved as can be seen by integrating the EoM once:

$$\mathbf{p} = M\mathbf{v}_s = \mathbf{p}_{\text{sf}} + \dot{\mathbf{p}}_{\text{in}}t, \quad (\text{C.4})$$

where  $p_{\text{sf}}$  is the momentum at the beginning of the radiative stage, also known as shell formation (see e.g. Kim & Ostriker 2015; Oku et al. 2022; Romano et al. 2024).

For a single explosion ( $\dot{\mathbf{p}}_{\text{in}} = 0$ ) the solution approaches the well-known momentum-conserving snowplow solution (Cioffi et al. 1988)

$$r_s \rightarrow \left( \frac{3p_{\text{sf}}t}{\pi\rho_0} \right)^{1/4}, \quad (\text{C.5})$$

while for continuously driven superbubbles ( $\dot{\mathbf{p}}_{\text{in}} > 0$ ) the solution approaches that of a momentum-driven wind (Oku et al. 2022; Lancaster et al. 2024)

$$r_s \rightarrow \left( \frac{3\dot{\mathbf{p}}_{\text{in}}t^2}{2\pi\rho_0} \right)^{1/4}. \quad (\text{C.6})$$

As for the adiabatic case, these results are stated in terms of the total momentum (injection-rate) over the whole sky.

Radiative SNRs are said to merge with the ISM once they have slowed down to the velocity dispersion of the ISM. The merging phase hosts rich phenomenology, such as SNR implosion (Slavin & Cox 1992; Romano et al. 2024), which requires a combined treatment of the bubble and the shell and is therefore outside of the model presented here.

The thin-shell approximation is a one-zone representation of SNR evolution and therefore by definition is unsuited for describing the interplay of the cold shell and the hot bubble. In order to describe e.g. the emergence of the reverse shock, the pressure-driven snowplow phase, or SN implosion after merging, a multi-zone extension to this model would be required, which explicitly models the coupled dynamics of the bubble-shell system. Such multi-zone calculations are outside the scope of this current work.

### Appendix D: Shape Tensor

We define the shape tensor as

$$S_{ij} = V_{\text{SNR}}^{-1} \int_{\text{SNR}} \left( \|\mathbf{x}\|^2 \delta_{ij} - x_i x_j \right) d^3\mathbf{x}. \quad (\text{D.1})$$

By assuming an approximately ellipsoidal shape, the three ellipsoidal radii, are defined by

$$r_i = \sqrt{2.5(\text{tr}(S) - 2S_i)}, \quad (\text{D.2})$$

where  $S_i$  are the eigenvalues of  $S_{ij}$  and  $\text{tr}(S)$  is the trace. The smallest, intermediate and largest eigenvalues correspond to the minor  $a$ , semi-major  $b$  and major  $c$  axis, respectively. The effective size of an SNR is the geometric mean of the three eigenvalues

$$r_{\text{eff}} = (abc)^{1/3}. \quad (\text{D.3})$$

To determine the alignment of the an SNR with respect to the galaxy, we measured the pitch angle  $\alpha$  of the major axis. As in the case of the shearing sphere, the semi-major axis aligns with the vertical direction and the minor axis is simply shifted by  $90^\circ$  relative to the major axis. The pitch angle is defined relative to the direction of galactic rotation, with  $\alpha = 90^\circ$  and  $\alpha = -90^\circ$  corresponding to the galactic center and anti-center, respectively.